Lattice Engineering with Surface Acoustic Waves

by

Mats Sahlman Powlowski

A thesis
presented to the University of Waterloo
in fulfillment of the
thesis requirement for the degree of
Master of Applied Science
in
Electrical and Computer Engineering

Waterloo, Ontario, Canada, 2018

© Mats Sahlman Powlowski 2018

I hereby declare that I am the sole author of this thesis. This is a true copy of the thesis, including any required final revisions, as accepted by my examiners.

I understand that my thesis may be made electronically available to the public.

Abstract

Quantum simulators are special purpose quantum computers designed to examine problems that are impossible to test with classical computers. They can be used to simulate problems in atomic physics, condensed matter physics, cosmology, high energy physics, nuclear physics and quantum chemistry, among other topics. In condensed matter physics, the simulators are composed of particles and a lattice structure containing the particles.

This thesis considers the use of exciton-polaritons as particles and surface acoustic waves to form the lattice potential. Exciton-polaritons are quasiparticles formed by the coherent mixture of photons and excitons in a semiconductor, with properties that are a combination of both components. Lattices of exciton-polaritons can be made by controlling the potential landscape for either the excitons or the photons.

This thesis covers two main topics: Surface acoustic waves are mechanical waves that propagate along the surface of a material. They can be simply generated via the inverse piezoelectric effect with interdigital transducers (IDTs) and can be designed to operate at frequencies, from several MHz to several GHz. They modulate the bandgap of the underlying material through the strain field that they carry, which can be used to trap excitons. The formation of potential landscapes for exciton-polaritons with surface acoustic waves has been demonstrated by another group, although their lattices were limited in scope.

1) I designed IDT layouts used to produce lattices that have not been previously demonstrated with surface acoustic waves. Numerical calculations were used to verify the validity of the design. Several pieces of test equipment both for the electrical and optical measurements were designed and built. 2) The designed devices were fabricated using both electron-beam and optical lithography and the quality of the resulting IDTs was quantified by S-parameter measurements. Observation of the lattices formed by the designed devices and the next steps required in implementing a quantum simulator are discussed.

Acknowledgements

I would like to thank my supervisor, Na Young Kim, for her guidance and for pushing me when I needed it.

I would like to thank Nathan Nelson-Fitzpatrick, Francois Sfigakis and Mohsen Asad for various discussions about fabrication that taught me a lot and helped me to overcome several pressing issues. I also appreciate Francois' help with the low temperature SAW velocity measurements. I would like to thank Kyung Choi, Sainath Motlakunta and Roberto Romero for help with milling PCB boards.

I would like to thank Roberto, Peter Sprenger and Brandon Buonacorsi for letting me borrow electrical test equipment. I would like to acknowledge the GaAs substrates and polariton samples that I received from Chris Deimert and Zbigniew Wasilewski.

Finally, I would like to thank my parents and my brother for their support, both before and during this degree.

Table of Contents

List of Figures **vii**

List of Tables **ix**

List of Abbreviations **x**

1 Introduction **1**

1.1 Context 1

1.2 Motivation 3

1.3 Structure of Thesis 4

2 Surface Acoustic Waves and Excitons **5**

2.1 Surface Acoustic Waves 5

2.2 Quantum Wells and Microcavities 8

3 Design and Simulation **11**

3.1 Device Design 11

3.2 Equipment Design 17

3.3 Simulations and Numerical Calculations 22

4 Device Fabrication **33**

4.1 Electron Beam Lithography 33

4.2 Optical Lithography 37

4.3 Troubleshooting Lithography Steps 39

4.4 Mesa Etching 41

4.5 ZnO Sputtering 42

5 Results **44**

5.1 IDT Quality Measurement 44

5.2 GaAs and ZnO/GaAs SAW Velocity Measurement 46

5.3 Optical Measurement of Polariton Devices 49

5.4 Microfluidic Lattice Formation Measurement 52

5.5 Future Work with Fabricated Devices 54

6 Conclusion **55**

6.1 Summary 55

6.2 Future Experiments 56

References **57**

APPENDICES **61**

A Triangular Lattice Calculations **62**

B Additional Strain Depth Equations and Constants **63**

C Parabolic Fitting Data for GaAs and ZnO/GaAs **64**

List of Figures

1.1 Quantum Simulator Representation 2

2.1 SAW Propagation 6

2.2 Crystal Axes of Anisotropic Piezoelectric Materials 6

2.3 Power Flow Angle 7

2.4 Quantum Well Band Diagram 8

2.5 G0299 Polariton Structure 10

3.1 IDT Designs 12

3.2 Mesa Concept Diagram 14

3.3 Lieb Lattice and Kagome Lattice Device Design 16

3.4 Wilkinson Divider Model 18

3.5 Simulated and Measured Results for Wilkinson Dividers 19

3.6 Room Temperature Power Divider PCB 20

3.7 Preparation of Cryostat for RF Measurements 21

3.8 Square SAW Lattices 23

3.9 Square Lattice for Suspensions 25

3.10 Triangular Lattice for Suspensions 26

3.11 Depth Dependence of Strain 28

3.12 Depth Dependence of Electric Field 29

3.13 Depth Dependence of Bandgap Modulation 30

3.14 Simulation of SAW propagation through mesa 31

4.1 Full Device Fabrication Flow 34

4.2 IDTs fabricated with EBL 37

4.3 IDTs fabricated with MLA 39

4.4 Problems with IDT Fabrication 40

4.5 XRD spectra of ZnO. 43

4.6 ZnO/GaAs IDT Response Comparison 43

5.1 Examples of IDT Reflection and Transmission 45

5.2 Room Temperature Direction Dependent Velocity on gallium arsenide (GaAs) and zinc oxide (ZnO)/GaAs 47

5.3 Angular Dispersion of SAWs at cryogenic temperatures on GaAs and ZnO/GaAs 48

5.4 Temperature dependence of SAWs on GaAs and ZnO/GaAs 49

5.5 Optical Path for Polariton Measurements 50

5.6 Effect of SAWs on excitons in QWs. 51

5.7 Results of Lattice Formation with Latex Bead Suspension 52

5.8 Fluorescence Microscopy Setup 53

List of Tables

3.1 Wilkinson Divider Centre Frequency Data 20

4.1 EBL Exposure Parameters 35
4.2 DBR Etching Recipe 41

B.1 Constants for Elastic Strain Calculations 63

C.1 Fitting parameters for SAW velocity parabolic relations 64

List of Abbreviations

ADS Advanced Design System 18, 19

Al aluminum 40, 41

Al_2O_3 aluminum oxide 14

AlAs aluminum arsenide 9, 14, 15

AlGaAs aluminum gallium arsenide 14, 15, 30

AQS analog quantum simulator 1–3

Au gold 36, 39, 41

CCD charge-coupled device 50, 53

DBR distributed bragg reflector 3, 4, 8, 9, 14, 15, 30, 41

EBL electron beam lithography 13, 33, 35, 38–40, 55

GaAs gallium arsenide viii, 5–8, 13–15, 27, 29, 30, 33, 36, 37, 41–43, 45–49, 55, 56

GaP gallium phosphate 7

ICP inductively-coupled plasma 41

IDT interdigital transducer 5, 7, 11–17, 19, 29–31, 33, 34, 36–46, 48–56

IPA isopropyl alcohol 33, 35, 37, 38

$LiNbO_3$ lithium niobate 5, 6, 13, 15–17, 33, 39, 52–55

LPF long pass filter 53

MIBK methyl isobutyl ketone 35

MLA maskless aligner 37–39

NMP N-methyl-2-pyrrolidone 36

PCB printed circuit board 17, 18, 20, 22

PDMS polydimethylsiloxane 54

PL photoluminescence 15, 49–51

PMMA poly(methyl methacrylate) 33–36, 38, 41

pSAW pseudo-surface acoustic wave 6, 7, 47–49, 56

QCSE quantum confined Stark effect 29, 30

QNF Quantum NanoFab 33, 37

QW quantum well 3, 4, 8, 14, 15, 29, 30, 39, 50, 51, 55, 56

RF radio frequency 11, 19, 21, 41, 42

RIE reactive ion etching 41

RT room temperature 46–49

SAW surface acoustic wave 4–7, 11–16, 22, 23, 25–32, 42, 44–56, 63

Si silicon 7

SMA SubMiniature version A 18, 20, 21

SSMC Sub-SubMiniature version C 21, 22

Ti titanium 36, 39

XRD X-ray diffraction 42, 43

ZnO zinc oxide viii, 5, 11, 14, 33, 34, 37, 39–43, 46–49, 55, 56

Chapter 1

Introduction

1.1 Context

Quantum mechanics, while capable of describing many systems, is still not easy to simulate using a classical computer architecture, mainly due to the extreme memory requirements. The memory necessary to store all information about the system increases exponentially with system size; this is due to the need to "keep track of the probability amplitudes for all the possible classical configurations of the system" [1]. The task of representing the state of 40 spin-1/2 particles requires storing 2^{40} numbers, or ~3.2×10^{13} bits if single-precision is assumed [1]. This is a total of 4 TB of memory for only 40 particles, and would increase to 5×10^{12} TB by doubling the number of particles [1]! There are classical approaches available to simulate large quantum systems, like Monte Carlo algorithms [2], but due to the sign problem, they will only work well for problems where the functions in the phase space integrals do not change sign [1]. Notable examples of quantum systems effected by the sign problem include fermionic and frustrated systems [1].

The solution to this issue, as first proposed by Richard Feynman in 1982, is to build a computer of "elements which obey quantum mechanical laws" [3]. This is essentially a quantum computer, and indeed, a quantum computer can act as a universal quantum simulator, capable of simulating a problems in many diverse fields [4]. However, a universal quantum simulator is not necessary to perform quantum simulations; a "quantum device that mimics the evolution"[1] of the quantum system of interest in an analog manner, as shown in Fig. 1.1, can solve a set of specific problems. This is beneficial, as large quantum computers are still in development, but analog quantum simulator (AQS)s also have the

ability to simulate the entire target Hamiltonian, including unitary evolution. These analog systems can be realized with currently existing technologies.

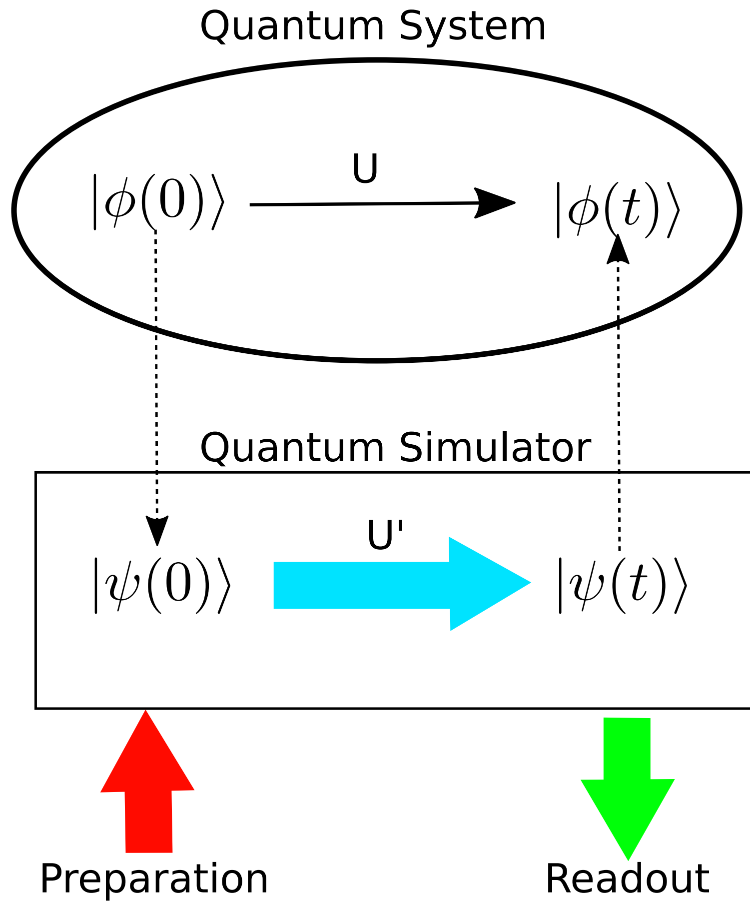

Figure 1.1: A schematic representation of a quantum simulator, based on Ref. [1]. The dashed arrows represent mappings between the quantum system and the simulator. U is a unitary transformation.

The AQS described in Fig. 1.1 is composed of three parts: 1) initial state $|\psi(0)\rangle$, 2) unitary transformation U, and 3) evolved state $|\psi(t)\rangle$. Each of these is mapped to its

corresponding component in the quantum system, which allows the measurement of $|\psi(t)\rangle$ to be used to determine the evolved state of the quantum system, $|\phi(t)\rangle$.

The AQS does not need to completely reproduce the dynamics of the quantum system, and in most AQSs, an effective many-body model of the quantum system is usually used [1]. Additionally, the AQS is somewhat error tolerant; if the goal of the simulation is to test if the system undergoes a quantum phase transition under specific conditions, a qualitative answer is sufficient [1]. However, care must be taken to ensure that the simulator is reliable so that the errors or imperfections are not interpreted as real results [5].

Quantum simulation can be used to study problems in many different fields, including but not limited to, atomic physics, condensed matter physics, cosmology, high energy physics, nuclear physics and quantum chemistry [1]. In this thesis, condensed matter problems are of greatest interest, in particular because they map well to the type of quantum simulator being fabricated. Many condensed matter problems can be studied with an array of particles and a lattice to control them, which act as a model of the lattice structure of solids that can be manipulated [1]. Condensed matter physics AQSs can be implemented in various physical platforms, including arrays of quantum dots, atoms, ions, nuclear and electronic spins, photons and superconducting circuits.

1.2 Motivation

The Kim group at the University of Waterloo has the experience and experimental setup necessary to measure and quantify exciton-polariton devices. Exciton-polaritons (called polaritons from here on) are quasiparticles that describe the mixture of a photon and an exciton in a semiconductor [6]. The excitons are confined to one or more quantum well (QW)s, which reduces the cross-sectional area where excitons can interact with photons. To increase the photon coupling to the QWs, they are placed in a cavity formed by distributed bragg reflector (DBR)s. A DBR is a dielectric mirror composed of alternating $\lambda/4$-thick layers of materials with different refractive indices [6].

AQSs made with polaritons are a subset of photonic AQSs, but are also effected by the excitons, which resemble an array of quantum dots when in a lattice [6]. This light-matter hybrid makes the polariton AQS distinct from other photonic AQSs. The excitons can be controlled by magnetic fields, unlike photons. The excitons also interact with each other via the Coulomb force, allowing many-body systems to be simulated.

There are several ways to make polariton lattices, which are based on creating a potential landscape for either the exciton or the photon modes [6]. Photonic potentials have

been generated by partial or complete etching of the cavity layer, design of the pump laser profile or a metallic thin film on the surface that modifies the effective cavity layer thickness [6]. Excitonic potentials have been generated by applying mechanical strain, electric fields or magnetic fields to the device [6]. With the majority of these methods, the strength of the potential landscape is determined by the fabrication method and cannot be modified after fabrication of the device.

One of the methods that does not suffer from this problem is the strain produced by surface acoustic wave (SAW)s propagating on the surface of the device. SAWs are acoustic waves that propagate along the surface of a material; however, due to the properties of SAWs, the SAW wavelength must practically be at least twice as large as the thickness of the top DBR and the effect of the strain at the QWs is limited by the top DBR thickness. In addition, the only 2D lattice pattern that has been demonstrated with SAWs is the square lattice [7].

The goal of this thesis is to design and demonstrate the formation of lattices of interest for quantum simulators. Of particular interest is the study of high T_c superconductivity and frustrated systems. Among the lattices used to study these phenomena are the 2D Lieb lattice (appears in high T_c cuprates [8]) and the kagome lattice (which has a high degree of frustration [9]).

1.3 Structure of Thesis

The remainder of this thesis is structured as follows. In chapter 2, descriptions are given of SAWs and exciton-polaritons. Chapter 3 covers how the devices and measurement equipment were designed. It contains the discussion of simulations or numerical calculations done for various aspects of the work. Chapter 4 details the fabrication techniques used to make the devices used for experiments and the results of that fabrication. Chapter 5 describes the results of several experiments, including work in measuring SAW velocity and and the progress made on observing the lattice formation. Chapter 6 summarizes the results and discusses the work that remains with this project.

Chapter 2

Surface Acoustic Waves and Excitons

The components representing the particles and the lattice of the planned quantum simulator are discussed.

2.1 Surface Acoustic Waves

Surface acoustic waves (SAWs) are phonons that propagate along the surface of a material. For the purposes of this work, waves with displacement normal to the surface, such as Rayleigh waves, are desired. Rayleigh waves consist of a transverse component (normal to the surface) and a longitudinal component, as shown in Fig. 2.1. They decay exponentially from the surface, with the majority of the energy contained within one wavelength of the surface. Since Rayleigh waves are the main wave of interest in this work, they will be referred to as SAWs from here on.

SAWs can be generated via the inverse piezoelectric effect by applying an varying electric field to a periodic array of metal strips known as an interdigital transducer (IDT). The period of the metal strips, also called fingers, is equivalent to the wavelength of the SAW. The characteristic acoustic velocity of the material and the wavelength define the resonant frequency of the SAW via the equation: $v = f\lambda$.

Piezoelectric materials can be either isotropic or anisotropic, which effects SAW propagation. In an isotropic material, such as *c*-axis oriented hexagonal ZnO [11, 12], the velocity is the same regardless of the direction of propagation. However, in an anisotropic material, such as zinc-blende GaAs [13, 14] or lithium niobate ($LiNbO_3$), there is an angular dispersion that must be taken into account. This is illustrated in Fig. 2.2. This angular

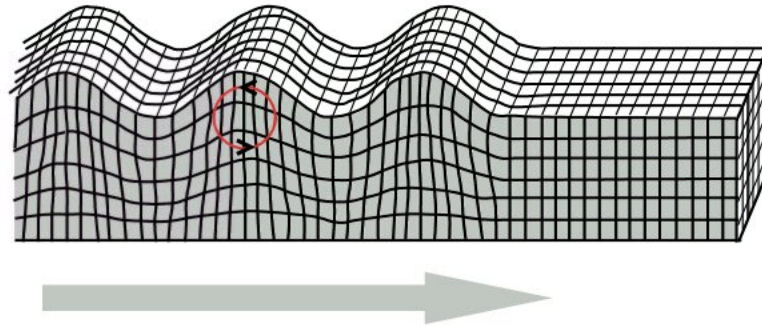

Figure 2.1: Image illustrating the propagation of a Rayleigh wave and the associated elliptical motion of a particle on the surface. The figure is from Ref. [10].

dispersion effects the velocity, the piezoelectric coupling constant k^2 and the power flow angle. Additionally, there are two possible propagation modes [13, 14], depending on the direction of propagation: (1) pure SAWs and (2) pseudo pseudo-surface acoustic wave (pSAW)s (or leaky SAWs) denoted as pSAWs.

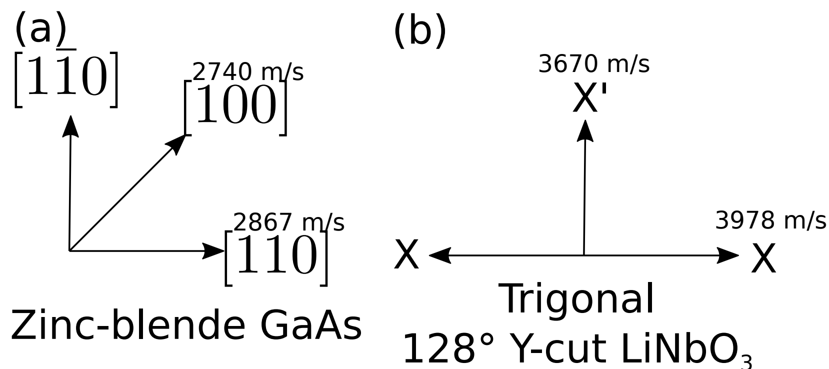

Figure 2.2: Crystal axes of anisotropic piezoelectric materials for (a) zinc-blende lattice of GaAs (b) trigonal lattice of $LiNbO_3$. Velocities in specific directions are indicated.

Pure SAWs act exactly as described above, and are thus simply called SAWs. pSAWs consist of a SAW component and a bulk transverse shear wave component [15]. In many

applications of SAWs, this is a disadvantage, as the bulk wave is equivalent to a loss of energy. In GaAs, the SAW propagates around the [100] direction, while the pSAW propagates around the [110] direction. The velocity dispersion is correlated to this division between the SAW and the pSAW, with two distinct regions in the velocity angular dispersion. The curvature in these regions shows if the wave propagation is autocollimating (concave-downward) or dispersive (concave-upward) around certain directions.

The concept of power flow angle is illustrated in Fig. 2.3(a). The power flow angle varies with direction, as shown in Fig. 2.3(b). This is a problem when the transmitted power needs to be maximized. The effect is more significant when the distance between IDTs is large compared to the aperture of the IDTs, since the power density profile travels further from the phase velocity axis.

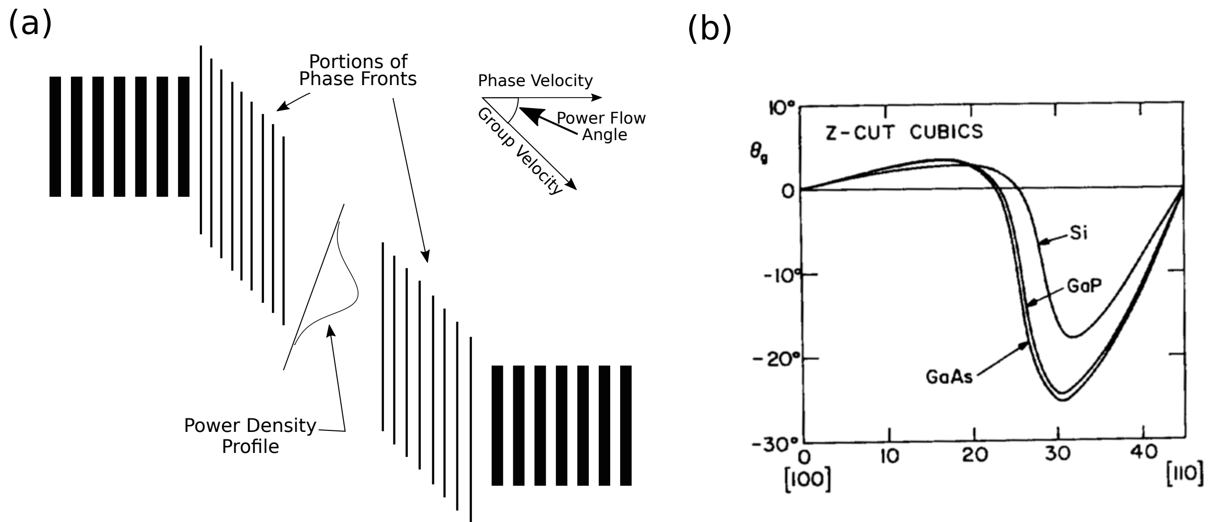

Figure 2.3: Power Flow Angle (a) Schematic showing concept of power flow angle, where phase and group velocity differ. Reproduced from Ref. [16]. (b) Power flow angle in (001)-cut Si, GaAs and GaP. Figure from Ref. [17]

The piezoelectric coupling constant has an angular dispersion as well, but this data is either not recorded or not shown in the literature. What this practically means is that the coupling strength varies with direction, so for identical IDTs, different amounts of power need to be applied to get the same amplitude of SAW.

2.2 Quantum Wells and Microcavities

Exciton-polaritons (called polaritons from here on) are quasiparticles that describe the mixture of a photon and an exciton in a semiconductor [6]. The excitons are confined to one or more QWs, in order to increase the exciton binding energy compared to the bulk exciton. The band diagram in Fig. 2.4 shows how a lower bandgap material surrounded by materials of higher bandgap will confine both electrons and holes. When the thickness d_w is comparable to or smaller than the de Broglie wavelength of the electrons and holes, energy levels are discrete in the confinement direction and the small bandgap material is called a QW. In a typical GaAs QW, the exciton binding energy is ~10 meV [18]. This allows these devices to be operated at temperatures up to 10 K without dissociation of the exciton by thermal energy.

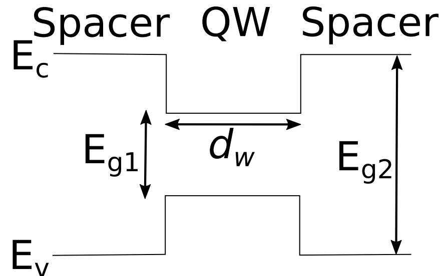

Figure 2.4: Band diagram of a QW, showing that a single QW can form traps in both the conduction and valence bands.

However, the finite thickness of the QW (7 nm in the polariton samples used in this thesis, as shown in Fig. 2.5) limits the interaction between the exciton and photon, due to the coherence length of the photon being larger than the QW thickness [18]. While making the photon coherence length shorter is not practical, this can be compensated by placing the QW(s) inside a microcavity that increases the photon lifetime. The mirrors that form the microcavity are DBRs, which consist of $\lambda/4$ layers of dielectric of alternating refractive indices. The use of multiple identical QWs inside the cavity increases the total interaction between excitons and photons. The total thickness of the cavity used is $\lambda/2$, limiting the number of QWs allowed.

The sample in Fig. 2.5 is designed to have a small quality factor Q; Q is ~4000 for 16.5 pairs in the top DBR and 20 pairs in the bottom DBR. The unbalanced DBR improves the photon extraction efficiency from the top of the structure. In order to increase Q, the number of layers in the DBRs should be increased. The increase in the number of

layers necessary for a larger Q is the primary reason that a low-Q cavity was used. The structure in Fig. 2.5 was the first such structure grown by Professor Zbigniew Wasilewski's group. Smaller Q structures take less time to grow and will be less effected by any potential instability in the flux. Once this initial structure is validated, larger Q structures can be attempted. Additionally, the nature of the fabrication done (involving etching the DBRs) and the uncertainty over how well the etched devices will work means that using large Q structures for the first generation of devices could lead to a waste of valuable samples.

The wavelength for the exact structure shown in Fig. 2.5 is 772.2 nm (assuming $n_{AlAs} = 2.97$ and $n_{AlGaAs} = 3.447$). However, the aluminum arsenide (AlAs) layers in the cavity were grown as a gradient in order to vary the cavity wavelength across the growth wafer. A total thickness variation of around ± 14.0 nm was expected across the entire wafer, which corresponds to a total variation of 83.82 nm in cavity wavelength. This provides a range of detunings between the exciton wavelength (~768 nm) and the cavity wavelength (gradient). The detuning determines the fraction of the polariton made up of photons and that made up of excitons, with a detuning of 0 eV representing 50% photons and 50% excitons.

Repeats	Layer Type	Material	Thickness (nm)
	Substrate	GaAs (SI)	
	Buffer	GaAs	200
20	Bragg Mirror	AlAs	65
	Bragg Mirror	$Al_{0.2}Ga_{0.8}As$	56
	Optical Cavity (graded)	AlAs	41
4	Quantum Well	GaAs	7
	Spacer	AlAs	3
	Optical Cavity	$Al_{0.2}Ga_{0.8}As$	32
	Optical Cavity (graded)	AlAs	40
3	Quantum Well	GaAs	7
	Spacer	AlAs	3
	Quantum Well	GaAs	7
	Optical Cavity (graded)	AlAs	40
	Optical Cavity	$Al_{0.2}Ga_{0.8}As$	32
4	Spacer	AlAs	3
	Quantum Well	GaAs	7
	Optical Cavity (graded)	AlAs	41
16	Bragg Mirror	$Al_{0.2}Ga_{0.8}As$	56
	Bragg Mirror	AlAs	65
	Bragg Mirror	$Al_{0.2}Ga_{0.8}As$	56
	Cap	GaAs	5

Figure 2.5: Structure of G0299 polariton wafer, used for polariton devices in this work. The wavelength for the exact thicknesses shown here is 772.2 nm. The Q is ~4000.

Chapter 3

Design and Simulation

The IDT design and layout necessary to form lattices such as the Lieb or kagome lattice is non-trivial. In this chapter, the idea for doing forming these lattices is discussed and calculations are performed to verify the validity of this approach. Several pieces of customized equipment are also necessary in order to use the designed SAW devices; the design and fabrication of this equipment is discussed.

3.1 Device Design

This section includes information about the design equations for the IDTs and how other considerations effected the choice of IDT parameters. The relevance of using a piezoelectric ZnO layer and a mesa are also discussed.

3.1.1 IDT Design

An IDT is a series of interlocked electrodes, referred to as fingers. An oscillating electrical signal, usually in the microwave or radio frequency (RF) range, is applied to opposite sides of the IDT to produce surface acoustic waves. As shown in Fig. 3.1, there are two possible IDT configurations, the single finger and double finger IDTs. In both designs, the periodicity of the fingers is equal to the wavelength of the SAW produced (λ_{SAW}). Assuming the most common metallization ratio (or metal filling factor) of 50%, the electrodes of the single finger design have a width and spacing of $\lambda_{\mathrm{SAW}}/4$, while in the double finger design, the width and spacing is $\lambda_{\mathrm{SAW}}/8$. While the single finger design is easier to fabricate

due to the larger dimensions, it also acts as a Bragg reflector, which can cause unwanted reflections. This is the primary reason for using a double finger IDT design.

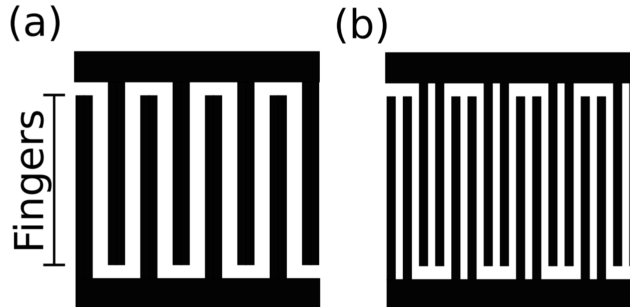

Figure 3.1: Possible finger layouts for IDTs. (a) Single finger IDT, with electrode and finger spacing of $\lambda_{\text{SAW}}/4$ for 50% metallization ratio. (b) Double finger IDT, with electrode and finger spacing of $\lambda_{\text{SAW}}/8$ for 50% metallization ratio.

The presence of the IDT on the surface changes the SAW velocity under the IDT, due to some combination of mass loading, electrical shorting at the surface and the acoustic velocity in the electrode material [19]. In order to be able to use the same frequency in all directions, the wavelength of any IDTs must match the velocity in that direction. These factors make the IDT design for this work an iterative process, where the velocity is measured by fabricating IDTs at different angles, which is then used to find the necessary wavelength. This is covered in section 5.2.

The number of finger pairs N_p (two successive electrodes in the single finger design, four in the double finger design) determines the bandwidth (BW) of the IDT, as shown in the following equation from Ref. [20]:

$$N_p = round\left(\frac{2}{BW} f_0\right) \tag{3.1}$$

where f_0 is the resonant frequency of the IDT and the *round* function rounds the argument to the nearest integer. The bandwidth is not considered to be an essential design parameter in this device, but it should be large enough to allow for differences due to fabrication.

The length of the SAW wavefronts is determined by the aperture height of the IDT, or the overlap between fingers on opposite sides of the IDT. The aperture height is always smaller than the length of the fingers, since there must be some separation between the fingers and the busbar on the opposite side.

The number of fingers, the aperture height and the piezoelectric coupling coefficient (direction dependent) affect the impedance of the IDT. In general, since the direction and bandwidth are usually set, the main parameter that can be tuned to match the IDT impedance to the source resistance is the aperture height. However, in this work, the aperture height is limited by the IDT layout used to produce the lattices and the limited space on the sample. In this case, the number of finger pairs is the free parameter, as the bandwidth is not of great importance. The aperture height (H_a) necessary for a given frequency changes with the number of finger pairs, as the following equation from Ref. [20] shows:

$$H_a = \frac{1}{R_{in}}\left(\frac{1}{2f_0C_sN_p}\right)\left(\frac{4k^2N_p}{(4k^2N_p)^2+\pi^2}\right) \tag{3.2}$$

where R_{in} is the input resistance of the source, k^2 is the piezoelectric coupling constant and C_s is the capacitance for a finger pair per unit length. When the number of finger pairs increases, the necessary aperture height decreases.

In this work, the wavelength was chosen to be 4 μm. This is near the diffraction limit of the optical measurement setup. Larger wavelengths, such as 8 μm, have been used for polariton devices [21], but as the wavelength increases, distances between lattice points start to become too large to be coupled.

For the devices discussed in section 5.2, an aperture of 100 μm and 70 finger pairs were used. This was mainly for fabrication reasons, as larger IDTs would have taken too long to fabricate with electron beam lithography (EBL). In subsequent devices, an aperture of 200 μm was used, to match the desired lattice formation area. The number of finger pairs was optimized based on the best S_{11} value. This resulted in 210 finger pairs.

The $LiNbO_3$ devices used for testing of the lattice formation devices proposed in section 3.1.3 are based on Ref. [22]. In order to try to keep the devices as similar as possible, nearly the same wavelength was chosen. One of the sets of IDTs is designed for a resonant frequency of 29 MHz, which gives wavelengths from 120 - 135 μm, depending on direction. The second set of IDTs is designed to double the frequency to 58 MHz. All of the IDTs have an aperture of 1.26 mm. The 29 MHz IDTs have 26 finger pairs and the 58 MHZ IDTs have 52 pairs; these pair numbers make the IDTs equal in size.

3.1.2 Other Device Considerations

The [100] direction in GaAs is non-piezoelectric [21], meaning that IDTs cannot be used to generate SAWs. However, this lack of piezoelectricity brings a benefit when used in

polariton devices, in that there is no associated piezoelectric field to dissociate the excitons [21]. In order to take advantage of this, a thin film of a piezoelectric material can be placed under the IDT. ZnO is a strong piezoelectric material that can be easily deposited by sputtering and has been used for this type of device before [21]. In addition, the SAW velocity on bulk ZnO is 2700 m/s, close to the maximum velocity of 2867 m/s in GaAs.

Many of the QW samples available for use in this work include one or more doped layers; normally, this makes generation of SAWs very difficult, since the electrical signal applied to the IDT couples to the doped layer, which dissipates the energy due to the high layer conductivity. This can be dealt with by screening the applied electrical signal from the doped layer with a metal film. By placing a metal film between the ZnO and the sample surface, it is possible to generate SAWs on a doped sample [23].

In order to increase the strength of the SAW at the QW, a mesa will be etched in the polariton sample. This is an idea that we have not seen in the literature, so the feasibility is unknown. A sketch of the mesa and the IDTs around it is shown in Fig. 3.2. A simulation used to explore this idea is presented in section 3.3.3. Polaritons will be able to exist under the mesa, but the SAW will be able to effect the QW from an effective distance from the surface.

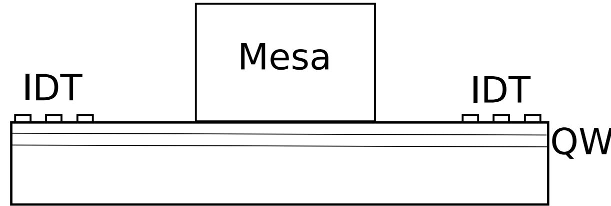

Figure 3.2: Diagram showing the relationship between the planned mesa and the IDTs around it. The QW is below the IDTs.

As a result of the strain not decreasing linearly with distance from the propagation surface, the height of the mesa necessary to maximize the potential induced by the SAW is not obvious. By calculating the dependence of the strain on distance from the surface, it is possible to choose an optimal height for the mesa. This is discussed in section 3.3.2.

There is one other factor to consider when deciding on the mesa height; how the etching will effect the DBR. The AlAs layers in the DBR should not be exposed to the environment to avoid oxidation and conversion to aluminum oxide (Al_2O_3). This means that when etching the mesa, the etch should stop inside aluminum gallium arsenide (AlGaAs) layer instead of the AlAs layer. Additionally, to be safe, the etch should not be designed to stop

exactly at the AlAs/AlGaAs barrier. The etch rate is unlikely to be accurate enough to achieve a target distance to within a fraction of a nanometer when the entire DBR is at least 2 μm thick and will require a faster etching rate. Even if this were possible, retaining an atomically flat surface after etching is unlikely, so some AlAs would be exposed.

The mesa size is important to determine as well. When using a mesa smaller than the beam spot size, the quality factor is effected by the distance from the base of the mesa to the QW [24]. To get around this, the mesa can be made bigger than the beam spot. The beam spot is less than 100 μm wide in the optical setup used, meaning that any mesa with a central area larger than 100 μm $\times$ 100 μm can be used. In this setup, a 200 μm $\times$ 200 μm square mesa is chosen, to allow for movement around the mesa and to avoid the edges of the SAWs.

3.1.3 IDT Layout

For lattice formation devices, the ideal situation is to have all SAWs propagating at the same velocity. Due to the crystal anisotropy of GaAs and $LiNbO_3$, this is only possible for square lattices, where the SAWs are perpendicular to each other. For GaAs, this is possible in any direction due to the velocity symmetry around the [110] and [100] directions. In this case, the [110] direction or the [100] direction are the best choices, as they are the directions with the strongest coupling and with no piezoelectric effect, respectively. For 128° Y-cut $LiNbO_3$, this is only possible at 45° from the X direction.

For the kagome lattice device, the IDTs need to be separated by 60°. This limits the number of possible directions, since one of the directions used must be an axis of symmetry. For GaAs, this means either the [110] direction and 30° from it or the [100] direction and 15° from the [110] direction. For $LiNbO_3$, this means either the X direction and 60° from it or the X'direction and 30° from the X direction. The choices made in this work are based on another factor. For GaAs, the lack of piezoelectric effect in the [100] direction makes it more appealing than the [110] direction, since dissociation of the excitons broadens the photoluminescence (PL) lines and reduces phase coherence [21]. For $LiNbO_3$, the similarity in velocity at 30° from the X direction and the X'direction make it a better choice than the X direction.

In order to make decorated lattices such as the Lieb lattice and the kagome lattice, an arrangement of IDTs around a central area is not sufficient. Inspiration was drawn from optical lattices for cold atoms; in Ref. [9], one wavelength is used to produce a standing triangular lattice, which is overlaid with a wavelength double the first one, in order to remove certain lattice points. IDTs with two or four fingers per period do not produce

even harmonics, while IDTs with three fingers per period do [25]. Taking advantage of this, two IDTs are placed in line with each other to produce two SAWs of different wavelengths along the same line. This idea is shown in Fig. 3.3 and examined numerically in section 3.3.1.

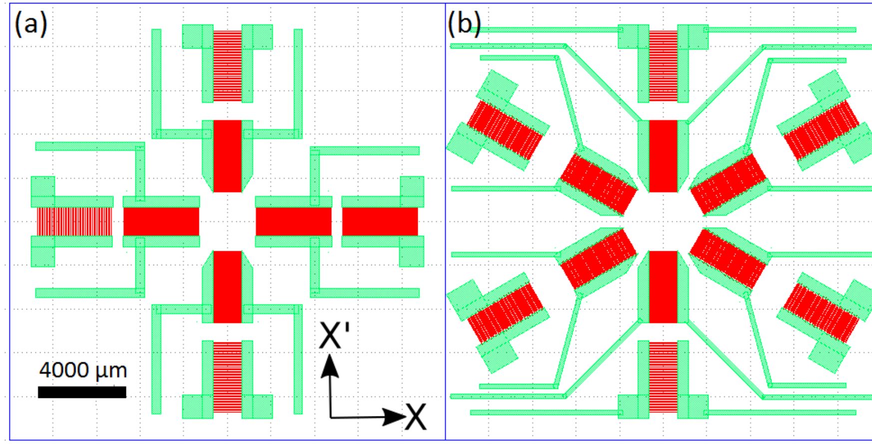

Figure 3.3: $LiNbO_3$ lattice formation device designs. (a)Lieb lattice device with IDTs in X and X'directions (b) Kagome lattice device. The smaller wavelength IDTs are closer to the centre, while the larger wavelength IDTs are closer to the edges of the device.

In order to form standing waves, two options are possible. The first is to place IDTs on opposite sides of the central area and apply equal signals to both IDTs. This is the approach that was followed due to its simple implementation. Another possibility is to use a single IDT with a reflector on the opposite side; this is useful in that it reduces the number of electrical connections necessary but it also requires high quality, low-loss reflectors. This approach is worth exploring in layouts with many IDTs and few available connections, a stage this work did not reach. A third possibility is to use a resonator, which can be made using shorted IDTs as reflectors; however, this approach is problematic when there are multiple wavelengths involved. The shorted IDT reflectors act as Bragg reflectors, meaning that they have a limited bandwidth; this means that multiple sets of reflectors would be needed to form resonators for all of the wavelengths. This approach is worth exploring for future work.

3.2 Equipment Design

The design of equipment necessary for the lattice formation is described here. This includes a power divider to form standing waves and adding new coaxial cables to an existing cryostat.

3.2.1 Wilkinson Power Divider

In order to generate standing waves, the best way of applying equivalent input signals on opposing IDTs is to use a power divider. The divider should also allow the input and both outputs to be matched. The simplest power divider, the resistive divider, has a very broad bandwidth, but suffers from a 6 dB loss, 3 dB of which are lost to the split and 3 dB of which are dissipated as heat. In a device where we want to have the maximum power available, this is not the best choice. Instead, use of a Wilkinson power divider allows for (theoretically) only 3 dB of loss, solely due to the 50:50 division of power.

This divider is designed for the $LiNbO_3$ devices. The problem with Wilkinson power dividers at low frequencies is that they require a quarter-wave transformer; in the case of a 60 MHz signal, this would be 69.7 cm on an FR4 printed circuit board (PCB), which is much too large for one divider, much less four or six of them. Instead, a lumped element Wilkinson divider can be used, the model of which is shown in Fig. 3.4. The equations to calculate the values of the inductors and capacitors are:

$$L = \frac{Z_0}{2\pi f} \tag{3.3}$$

$$C = \frac{1}{2\pi f Z_0} \tag{3.4}$$

where Z_0 is $\sqrt{2}$ times the regular line impedance (50 Ω) and f is the centre frequency.

Taking the closest values for commercially available components, a 29 MHz signal requires L = 390 nH and C = 75 pF and a 58 MHz signal half that (L = 195 nH, C = 37.5 pF). However, there is no 195 nH inductor available, so instead of using one inductor, two will be placed in parallel. For the capacitor, there are no 37.5 pF capacitors and few 37 pF or 38 pF capacitors, so two capacitors will be placed in series.

Using these real inductor and capacitor values, the reflection at the input (S_{11}), the transmission from the input to the output (S_{31}, S_{21}) and the isolation between the two output ports (S_{32}) are shown in Fig. 3.5(a) and (c) for signals of 29 MHz and 58 MHz,

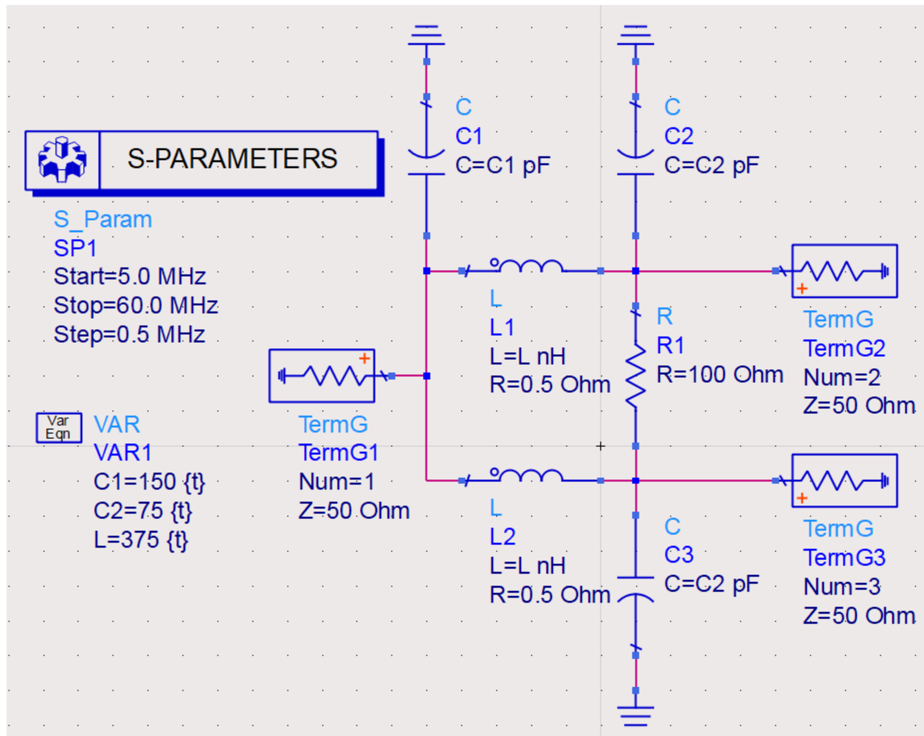

Figure 3.4: Model of lumped element Wilkinson power divider, drawn in Keysight's ADS. C2 represents two C1 capacitors in parallel. The capacitor and inductor design values shown are for a 30 MHz signal.

respectively. S_{11} is a measure of how much of the input power is reflected; it should be as small as possible, but 20 dB is sufficient, as that is equivalent to 1% reflected power. S_{32} is the isolation between the two output ports; it should also be as small as possible (20 dB is reasonable). S_{31} and S_{21} are ideally 3 dB, equivalent to the power at each output port being half of the power at the input.

The full Wilkinson divider PCB, with three 29 MHz dividers and three 58 MHz dividers, is shown in Fig. 3.6. SubMiniature version A (SMA) connectors are used connect the PCB to external components. The measured results of these dividers are shown in Fig. 3.5(b) and (d) for signals of 29 MHz and 58 MHz, respectively. The measured results are slightly off in both frequency and amplitude compared to the simulated results, as shown in Table 3.1. The 29 MHz divider centre frequency is off by less than 0.5 MHz, while the transmission loss is 0.35 dB worse than expected. The 58 MHz divider, is significantly worse, with the

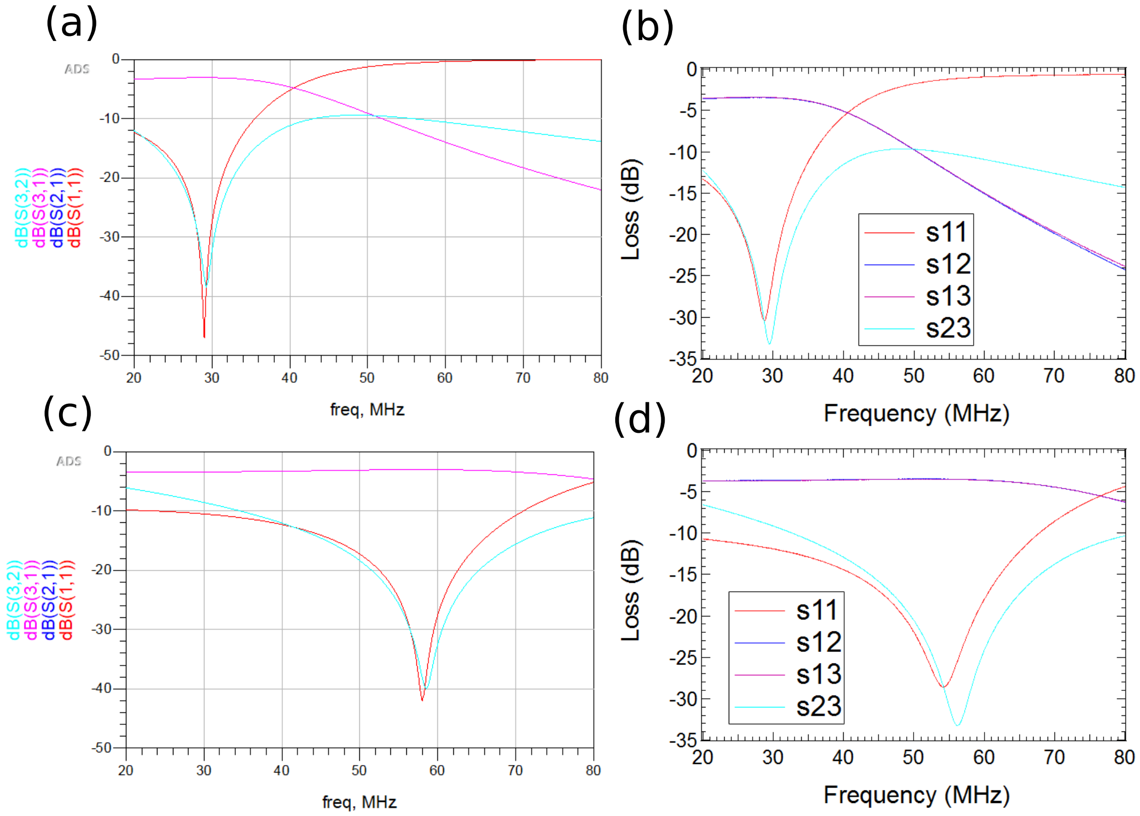

Figure 3.5: The reflection at the input (S_{11}), transmission from input to the outputs (S_{31}, S_{21}) and isolation between the two outputs (S_{32}) for the designed Wilkinson dividers. (a) Simulation results from ADS for 29 MHz Wilkinson divider. (b) Measured results of 29 MHz Wilkinson divider. (c) Simulation results from ADS for 58 MHz Wilkinson divider. (d) Measured results of 58 MHz Wilkinson divider.

S_{11} centre frequency off by 3.7 MHz and the transmission 0.52 dB worse than expected. However, at 58 MHz, the S_{11} is still -21.42 dB and the S_{32} is -29.07 dB, which are still acceptable values, as mentioned above.

3.2.2 Coaxial Cables in Wet Cryostat

In order to apply RF signals to the IDTs in a cryostat, cables with low attenuation at RF frequencies are necessary. The cryostat in the optical setup was not originally equipped

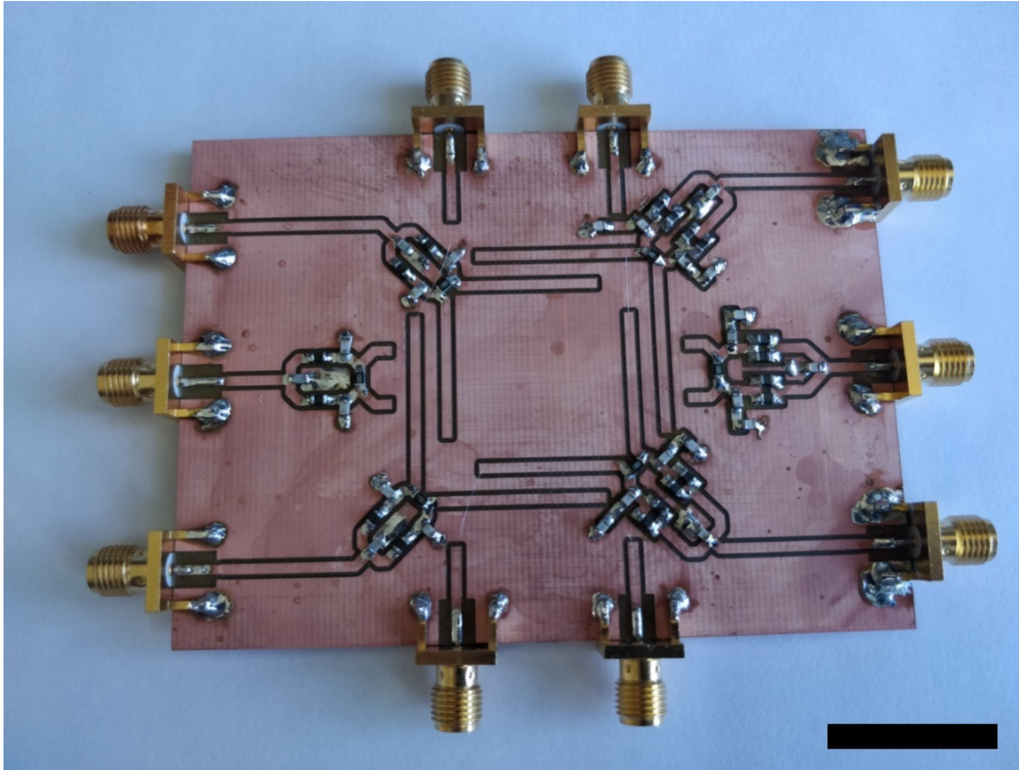

Figure 3.6: The final Wilkinson power divider PCB. The SMA connectors on the top and bottom are for testing the power dividers, while the SMA connectors on the left and right are the Wilkinson divider inputs. The dividers on the left are 29 MHz dividers, those on the right are 58 MHz dividers. Scale bar is 2 cm.

Table 3.1: Numerical results of 29 MHz and 58 MHz Wilkinson dividers at their centre frequencies, both for simulated and measured data

Result	S_{11} (MHz)	S_{11} (dB)	$S_2 1$ (MHz)	S_{21} (dB)	S_{32} (MHz)	S_{32} (dB)
29 MHz sim.	29.0	-47.02	29.0	-3.07	29.0	-36.81
29 MHz meas.	28.78	-30.37	29.0	-3.42	29.45	-33.2
58 MHz sim.	58.0	-42.0	58.0	-3.04	58.0	-38.09
58 MHz meas.	54.31	-28.5	58.0	-3.56	56.15	-33.2

with these cables, so they had to be inserted manually. Semi-rigid coaxial cables (UT-

085B-SS from Microstock Inc.) were chosen for this task based on previous experience with coaxial cables in cryostats. In order to connect them to the environment without losing thermal isolation, hermetic SMA connectors were inserted in a plate, as shown on the left in Fig. 3.7.

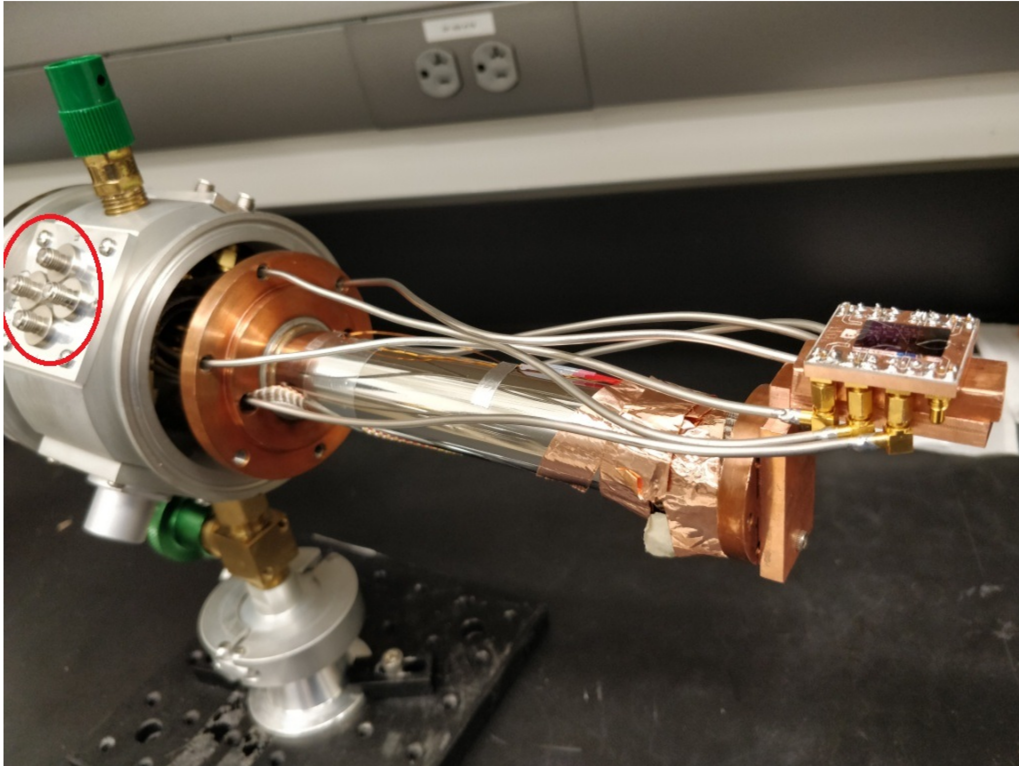

Figure 3.7: Installation of coaxial cables for RF signals in cryostat. They are connected to the sample holder via SSMC connectors. The hermetic SMA connectors are indicated with a red circle.

Right-angled SMA connectors were soldered onto one end of the coaxial cables and attached to the hermetic SMA connectors. The coaxial cables were threaded through the holes in the copper plate shown in Fig. 3.7. The problem with this is that the bending range of the coaxial cables is limited, which prevented the use of one of the holes in the plate. Additionally, in order to attach the coaxial cables to the hermetic SMA connectors, the hermetic SMA plate needs to be lifted off the cryostat body. Due to the semi-rigid cables, only three coaxial connectors could be installed for each plate. This led to a total of six coaxial cables, when eight cables was the original plan.

SSMC connectors were soldered to the other end of the coaxial cables and connected to a high frequency laminate PCB made of Rogers RT/Duroid 6002, as shown on the right in Fig. 3.7. In order to change the sample, the coaxial cables are disconnected and the screws holding the PCB on the mounting bracket are removed. The sample can then be replaced and wirebonded to the coplanar waveguide lines on the PCB.

3.3 Simulations and Numerical Calculations

Numerical Calculations are used to examine the feasibility of the design. This includes calculations for the expected results of the Lieb and kagome device configurations, the depth-dependent effect of the strain carried by the SAW and a simulation of the feasibility of the mesa approach.

3.3.1 Lattice Generation Calculation

In order to test the concept behind the lattice generation devices in Fig. 3.3, numerical calculations were done. These consist of a superposition of the standing wave pattern for the short-wavelength lattice and the long-wavelength pattern of the same type. For the Lieb lattice, this means square lattices, while for the kagome lattice, this requires triangular lattices. In all of these cases, velocity is assumed to be isotropic, which it is not in the real SAW devices.

For SAWs, the equation for a square lattice is as follows:

$$\psi = A\sin(kx + \phi_1)\cos(ky + \phi_2)\cos(\omega t) \tag{3.5}$$

where $k = 2\pi/\lambda$, A is an arbitrary amplitude assumed to be 1, $\omega = 2\pi f$ and ϕ_1 and ϕ_2 are phase offsets. At time $t = 0$, this produces the square lattice shown in Fig. 3.8(a), which is shown with absolute amplitude to highlight the nodal lines. For this lattice, $\lambda = 100$ μm and periodicity is $\lambda/2$, or 50 μm. When adding a lattice formed using the same equation but with a wavelength of 200 μm and offsets of $\phi_1 = \pi/2$, $\phi_2 = \pi/4$, the resulting potential pattern is shown in Fig. 3.8(b).

This does seem like a Lieb lattice is being formed, if particles are assumed to gather at particular nodes rather than all along the nodal lines.

Due to problems with seeing a response from the polariton devices (discussed in section 5.3), a different particle system was explored. Due to the small amount of time remaining

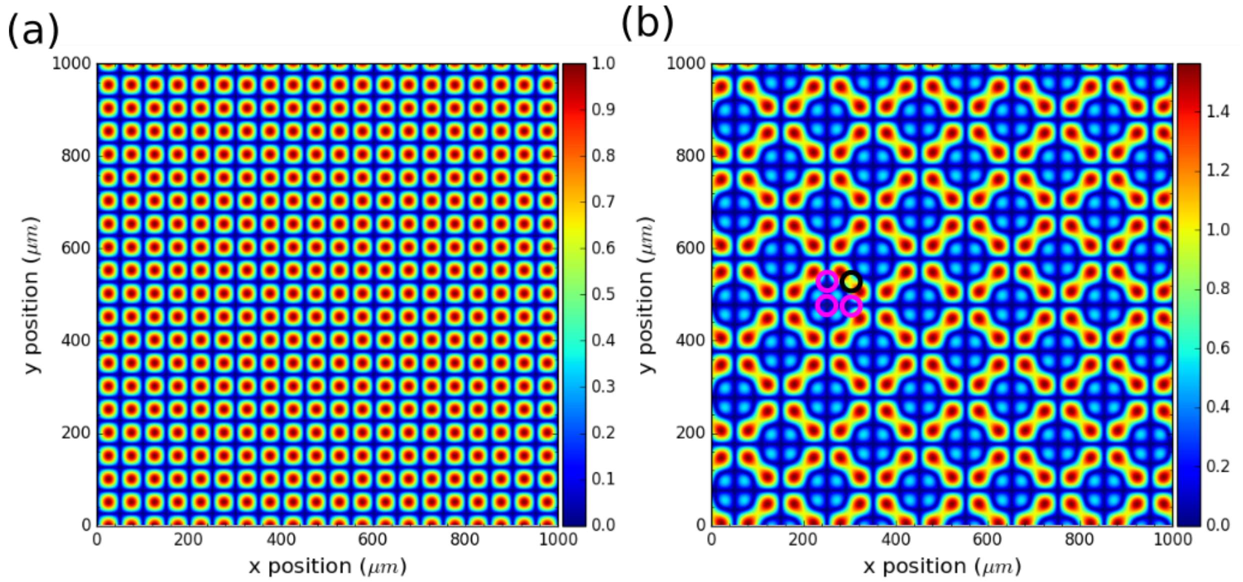

Figure 3.8: Lattices formed from plane waves perpendicular to each other. All amplitudes are absolute values. (a) Square lattice formed by waves with wavelength $\lambda = 100$ μm. (b) Lattice formed by superposition of square lattices with wavelengths of 100 μm and 200 μm. The magenta circles show the locations of the three sublattices in the Lieb unit cell and the black circle shows the missing sublattice.

to complete this work, the criteria for this system were that measurements could be made without necessitating significant changes to the lab setup and that the system was simple to set up. The system that was selected was a microfluidic system, based on Ref. [22]. In this system, small objects are suspended in a fluid and the SAWs create a potential in the fluid. The suspended objects can be living or non-living objects, including cells and small organisms [26]. Non-living particles such as latex beads are faster to acquire and do not have a limited shelf-life like living organisms. They are available in diameters ranging from 0.5 μm to 10 μm.

The standing wave pattern on the substrate does not translate directly to the standing wave pattern seen in suspensions of particles, such as in Ref. [22]. The SAWs leak into the suspension and create standing-waves of pressure that trap the particles, which also adds terms to account for the interaction between the fluid and the particles. The equations for

a square standing wave pattern, adapted from Ref. [27] and [28], are as follows:

$$\begin{aligned} PE =& \frac{B_f}{4}((A_x \sin(kx))^2 + (A_y \sin(ky))^2 + \\ &+ (2A_xA_y \sin(kx)) \sin(ky) \cos(\phi)) \end{aligned} \tag{3.6}$$

$$KE = \frac{B_f}{4}((A_x \cos(kx))^2 + (A_x \cos(ky))^2) \tag{3.7}$$

$$\psi = \frac{B_f - B_p}{B_f} PE - 3\frac{\rho_p - \rho_f}{\rho_f + 2\rho_p} KE \tag{3.8}$$

where PE is the potential energy, KE is the kinetic energy, ϕ is a phase offset, B_f (B_p) is the compressibility of the fluid (particle) and ρ_f (ρ_p) is the density of the fluid (particle). In these calculations, water and latex beads are assumed, which use values of $B_f = 4.45\times10^{-10}$ Pa^{-1}, $B_p = 2.38 \times 10^{-10}$ Pa^{-1}, $\rho_f = 1000$ kg/m^3 and $\rho_p = 1050$ kg/m^3.

Using these equations, a square lattice pattern is produced, as shown in Fig. 3.9(a) for a wavelength of $\lambda = 100$ μm and $\phi = \pi/2$. Unlike the pattern shown in Fig. 3.8, the absolute value is not taken here, with trapping occurring at the lowest points in the potential. When $\phi = 0$ is used, the result is shown in Fig. 3.9(b). When the square lattices are superposed with a square lattice with $\lambda = 200$ μm and the results are shown in Fig. 3.9(c) and (d).

Both of the lattices in Fig. 3.9(c) and (d) appear to be Lieb lattices. Both may be useful, as they have different potential landscapes.

Using the same principle, calculations were also done for triangular lattices. The triangular lattice is formed using one wave along the x-axis and two waves propagating at $\pi/3$ and $-\pi/3$ from the x-axis. The equations are given in Appendix A. The triangular lattice formed by waves of $\lambda = 100$ μm is shown in Fig. 3.10(a). When the amplitude of the wave along the x-axis is 1.75$\times$ larger than the other two waves, the lattice formed is shown in Fig. 3.10(b).

As with the Lieb lattice, the superposition of lattices formed with wavelengths of 100 μm and 200 μm is expected to produce a kagome lattice. The result of using the 100 μm lattices in Fig. 3.10(a) and (b) to form kagome lattices is shown in Fig. 3.10(c) and (d), respectively. While it is possible that concept will produce a triangular and a kagome lattice, the calculation results are unclear. The potential is not equal for all of the nodal points, starting with the triangular lattice. This should work with latex beads [27], but it is not assured.

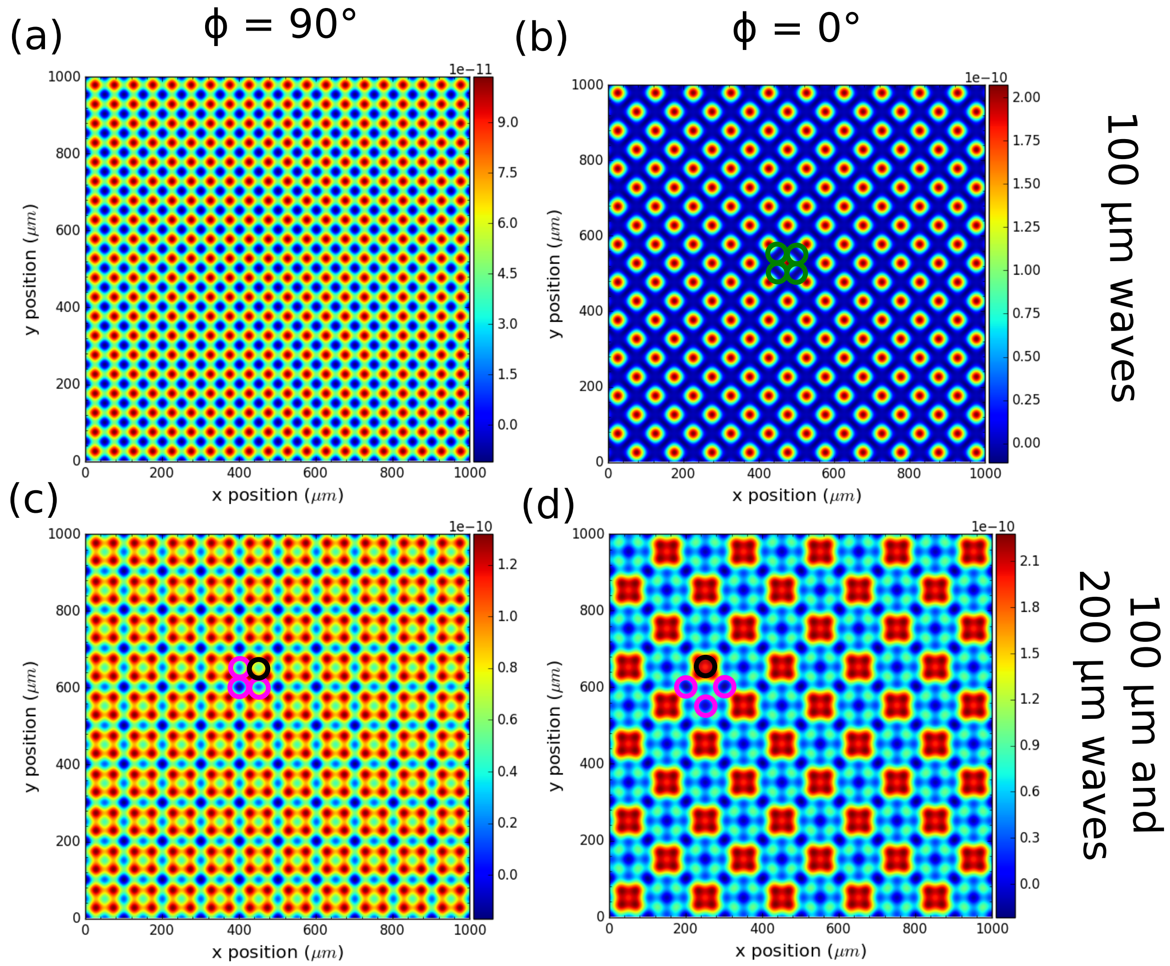

Figure 3.9: Standing wave lattices for latex particles suspended in water. (a) Square lattice formed by SAWs with wavelength 100 μm, with $\phi = \pi/2$. (b) Same as (a), but with $\phi = 0$. Green circles indicate lattice points. (c) Superposition of square lattices formed by 100 μm and 200 μm SAWs, using lattice in (a). The 200 μm lattice has 3/4 of amplitude of 100 μm lattice. (d) Superposition of square lattices of equal amplitude, formed by 100 μm and 200 μm SAWs, using $\phi = \pi/2$ for the 100 μm lattice and $\phi = \pi$ for the 200 μm lattice. The magenta circles show the locations of the three sublattices in the Lieb unit cell and the black circle shows the missing sublattice.

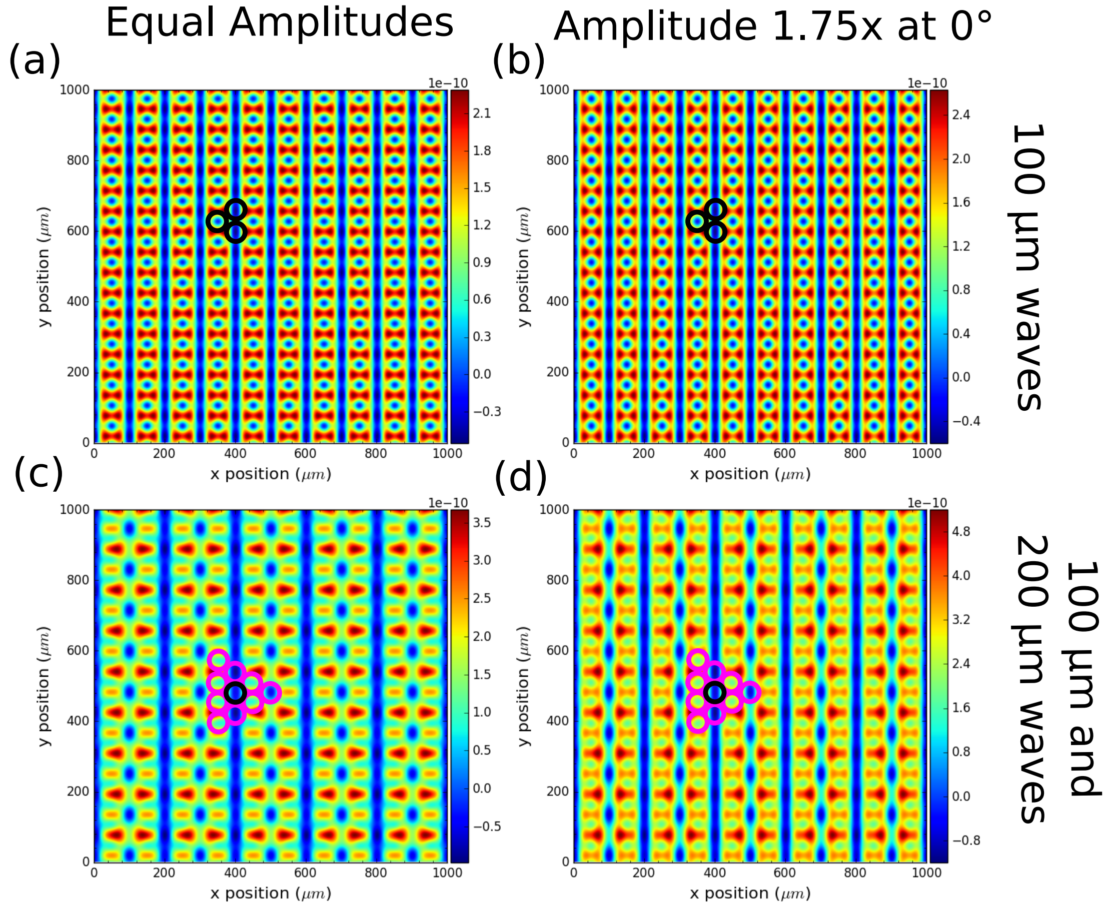

Figure 3.10: Standing wave lattices for latex particles suspended in water. (a) Triangular lattice formed by SAWs with $\lambda = 100$ μm. (b) Same lattice as in (a), but with the SAW along the x-axis having 1.75× the amplitude of the other two waves. The black circles indicate the lattice points. (c) Kagome lattice formed by superposition of 100 μm and 200 μm lattices of the type shown (a). (d) Same as (c), but formed with lattices of type shown in (b). The magenta circles show the locations of the points in the kagome shape and the black circle shows the missing point.

3.3.2 Strain field penetration as function of depth

In order to create a potential field for exciton-polaritons, there are two possibilities; either the photonic potential or the excitonic potential can be modulated. SAWs primarily

modulate the excitonic potential through periodic modulation of the band structure of the material on which it propagates [29]. This is done either by the strain field produced by the SAW itself or by the piezoelectric field that all SAWs propagating in a piezoelectric direction generate.

The piezoelectric field parallel to the direction of propagation (F_x) induces a modulation ($= \lambda_{\text{SAW}}/(2\pi)F_x$) that is much larger than the strain modulation, but it can dissociate excitons at high powers [21]. The non-piezoelectric [100] direction in GaAs is preferred to the [110] direction because it does not generate a piezoelectric field. If the [100] direction is used, the modulation of the band structure is done solely by the strain field.

The strength of the strain field decreases with the amplitude of the SAW, but the decrease is not linear. Elastic theory can be used to calculate the strength of the strain field as a function of distance from the surface. Additionally, the electric field and the bandgap modulations can be calculated. The equations given below are all taken from Ref. [29], with smaller equations and constants appearing in Appendix B. All calculations assume pure GaAs and are done for the piezoelectric direction, as the modulation due to strain in the piezoelectric and non-piezoelectric only differ slightly in magnitude [21].

Equations (3.9)-(3.12) are used to calculate the strain in the direction of propagation (x) and into the substrate (z). Strain ε_{ij} is given by $1/2(\partial_i u_j + \partial_j u_i)$, where u is the displacement. Equation (3.12) gives the strain along the direction of propagation (xx) and into the substrate (zz), as a function of position x and time t on the surface. It is plotted when $x = 0.75\lambda$ and $t = 0$ in Fig. 3.11, for GaAs with a 4 μm SAW at a power density of 100 W/m.

$$A_{ph} = \sqrt{\frac{k_{SAW}}{2\rho\nu_{SAW}^3}P_l} \tag{3.9}$$

$$\phi_z(z) = e^{-\Omega_R k_{SAW} z - i\phi_R} \tag{3.10}$$

$$\hat{\varepsilon}(z) = \begin{pmatrix} \tilde{\varepsilon}_{xx} \\ 0 \\ \tilde{\varepsilon}_{zz} \\ 0 \\ 2\tilde{\varepsilon}_{xz} \\ 0 \end{pmatrix} = 2C \begin{pmatrix} iRe[\phi_z(z)] \\ 0 \\ iRe[\gamma_R \Omega_R \phi_z(z)] \\ 0 \\ Re[(\gamma_R - \Omega_R)\phi_z(z)] \\ 0 \end{pmatrix} \tag{3.11}$$

$$\varepsilon(\vec{r}, t) = A_{ph}[\hat{\varepsilon}(z)e^{i\varphi_{SAW}} + \hat{\varepsilon}^*(z)e^{-i\varphi_{SAW}}] \tag{3.12}$$

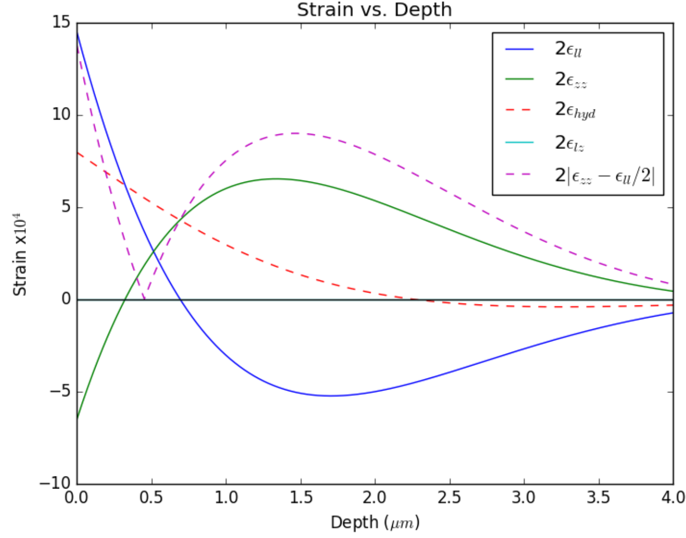

Figure 3.11: Dependence of strain on distance from the surface for a 4 μm SAW with power density of 100 W/m.

where P_l is the power density, ν_{SAW} is the SAW velocity and k_{SAW} is the SAW wavenumber.

Equations (3.13) - (3.16) are used to calculate the piezoelectric potential carried by the SAW, with the electric fields calculated as derivatives of the potential (Appendix B). The electric fields for a 4 μm SAW with power density of 100 W/m are shown in Fig. 3.12 at $x = 0.75\lambda$ and $t = 0$.

$$A_1 = \frac{\gamma_R - 2\Omega_R}{\Omega_R^2 - 1} \tag{3.13}$$

$$A_2 = -\frac{2}{1+\epsilon^{-1}}[\cos\phi_R + \epsilon^{-1}Re(A_1 e^{-i\phi_R}) + Re(\Omega_R A_1 e^{-i\phi_R})] \tag{3.14}$$

$$\tilde{\Phi}_{SAW}(z) = i\frac{Ce_{14}}{k_{SAW}\epsilon_0\epsilon}[(A_1 e^{-\Omega_R k_{SAW} z - i\phi_R} + A_1^* e^{-\Omega_R^* k_{SAW} z + i\phi_R^*}) + A_2 e^{-k_{SAW} z}] \tag{3.15}$$

$$\Phi_{SAW}(\vec{r}, t) = A_{ph}[\tilde{\Phi}_{SAW}(z)e^{i\varphi_{SAW}} + \tilde{\Phi}_{SAW}^*(z)e^{-i\varphi_{SAW}}] \tag{3.16}$$

where e_{14} is the piezoelectric coefficient of zinc-blende lattice structures and ϵ is the relative permittivity.

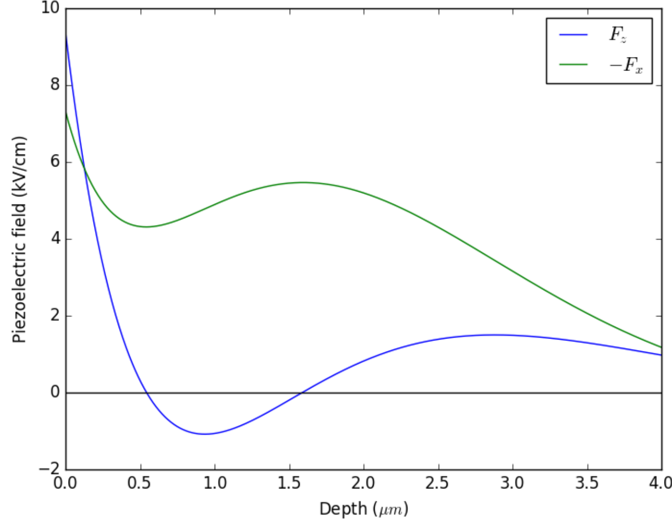

Figure 3.12: Dependence of electric field on distance from the surface for a 4 μm SAW with power density 100 W/m. x is the direction of propagation and z is into the substrate. $-F_x$ is used allow the electric field strengths to be compared.

Equations (3.17) and (3.18) are used to calculate the bandgap modulation due to strain and the quantum confined Stark effect (QCSE), respectively. In equation (3.17), the plus is for heavy holes (hh) and the minus is for light holes (lh). The QCSE requires a QW thickness (d_w), which in this case is taken as 7 nm. The results using a 4 μm SAW with power density of 100 W/m are shown in Fig. 3.13. As with the strain calculations, $x = 0.75\lambda$ and $t = 0$.

$$M_{dp}^{(g)} = \frac{A_{ph}}{E_g}[(a_{CB} + a_{VB})(\tilde{\varepsilon}_{xx} + \tilde{\varepsilon}_{zz}) \pm b_{VB}(\tilde{\varepsilon}_{zz} - \frac{\tilde{\varepsilon}_{xx}}{2})] \tag{3.17}$$

$$M_{QCSE} = \frac{d_w|F(z)|_{max}}{2E_g} \tag{3.18}$$

where a_{CB} and a_{VB} are the hydrostatic deformation potentials for the conduction and valence bands, respectively, and b_{VB} is valence band uniaxial deformation potential. In most cases, a_{CB} and b_{VB} cause the majority of the modulation of the conductance and valence bands, respectively. For GaAs, a_{CB} = -8.6 eV, a_{VB} = 0.4 eV and b_{VB} = -2.0 eV.

Figure 3.13 shows where the IDT should be located relative to the QWs. As expected, the modulation is larger closer to the surface. However, the peak of the hh modulation is

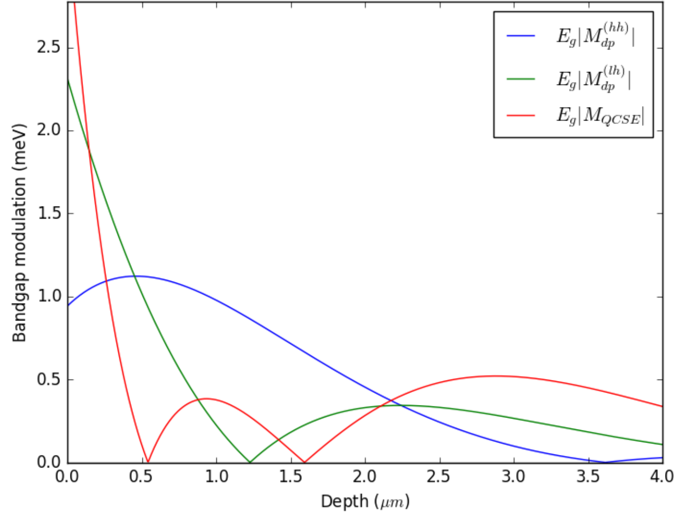

Figure 3.13: Dependence of bandgap modulation on distance from the surface for a 4 μm SAW with power density 100 W/m. The thickness of the QW used for the QCSE calculation is 7 nm. The absolute value of the modulation is shown to compare the strength of modulation of each type.

actually around 0.5 μm or 0.125λ. Ideally, QWs should be exposed to as uniform a bandgap modulation as possible, so the IDTs should be a distance of 450 nm from the centre of the microcavity. This is equivalent to etching 1662 nm of the G0299 sample shown in Fig. 2.5, leaving behind two and a half DBR layers topped with an AlGaAs layer 66% of the regular 56 nm thickness. In the polariton device made for this thesis, 1951 nm was etched, based on earlier calculations of the best location.

3.3.3 Mesa Simulation

COMSOL simulations were done in order to determine the feasibility of SAWs propagating through a mesa. The model is shown in Fig. 3.14(a). In this model, a SAW with $\lambda = 40$ μm propagates on GaAs. In order to match the intended mesa height, the mesa is h = $\lambda/2$ high. The mesa is L = 7λ long. The displacement in the z-direction (into the substrate) is shown along the centre of the IDT in Fig. 3.14(b) after time = 13.6T, where T is 1/71.7 MHz = 13.95 ns. This appears to show the SAW propagating through the mesa, while maintaining the same shape as outside the mesa.

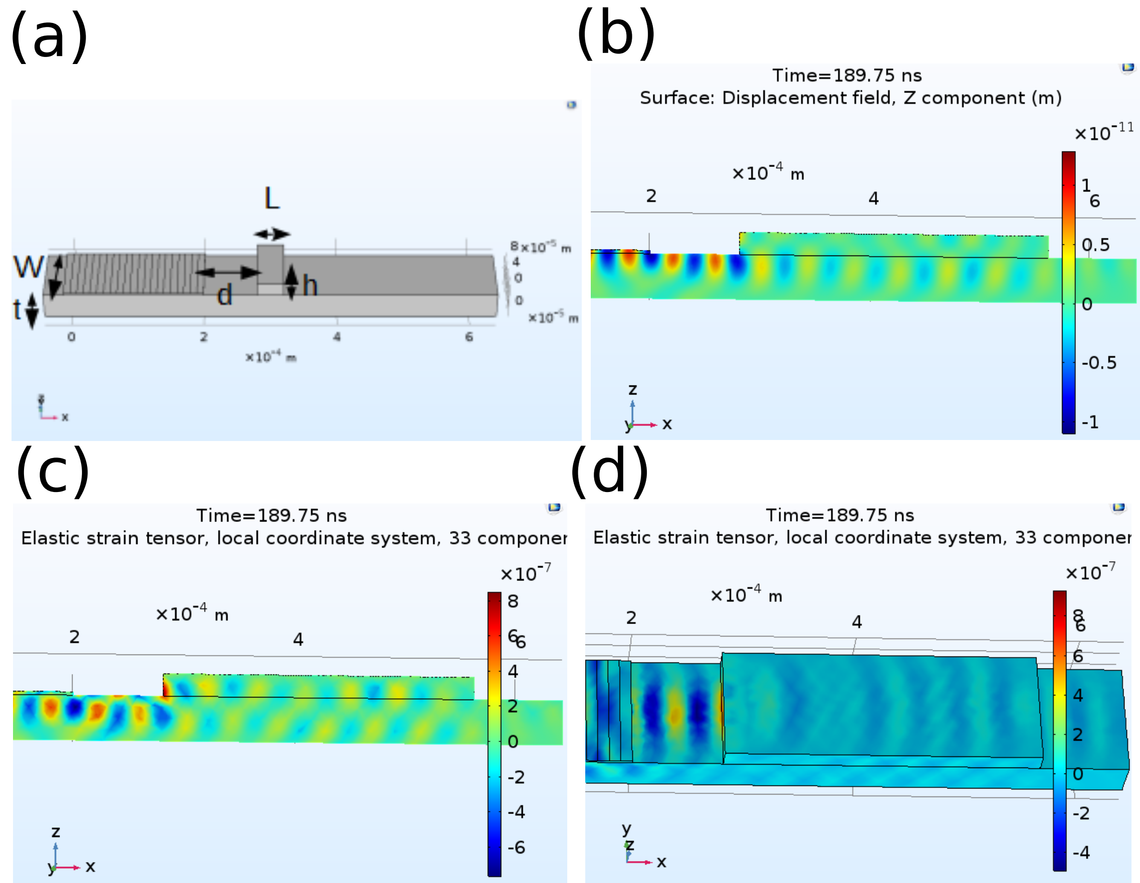

Figure 3.14: COMSOL simulation of a mesa in the path of a travelling SAW. (a) The COMSOL model, shown with wavelength $\lambda = 40\ \mu$m, finger width $W = 2.5\lambda$, substrate thickness $t = 1\lambda$, distance to mesa $d = 2.25\lambda$, mesa length $L = 1\lambda$ and mesa height $h = 0.5\lambda$. Models used in (b) - (d) also use these values, except that $L = 7\lambda$. (b) Displacement into the substrate, shown along the centre line of the IDT. (c) Elastic strain into the substrate, shown along the centre line of the IDT. (d) 3D view of elastic strain shown in (c).

Figures 3.14(c) and (d) show the elastic strain in the zz direction, or into the substrate, both along the centre of the IDT and in 3D. These also seemingly indicate that the SAW propagates through the mesa. The strain appears to be weaker while passing under the mesa, which may be due to the SAW energy also propagating through the mesa itself.

The weakening may also be due to some portion of the SAW being reflected; it is not possible to distinguish from the results in Fig. 3.14 if there are reflections. Reflections would be caused by a mismatch in acoustic impedance; the acoustic impedance of a material is equal to the density times the speed of sound in the material. In this model, the mesa and the substrate are made of the same material, so the mismatch could only be caused by the difference between the air above the substrate and the mesa. The air is not included in this model, so there should not any reflections due to acoustic impedance mismatch in Fig. 3.14. If there is an impedance mismatch in the real system, it is difficult to do anything about it, since the mismatch is caused by an unavoidable difference in materials.

The surface waves from an earthquake passing through a building was considered as a potential model for the mesa system. However, there are several features that differentiate the mesa from a building. Buildings are primarily empty and require horizontal structures such as the floors and the roof to withstand lateral forces caused by the earthquake, whereas the mesa is solid. Additionally, the mesa is a growth from the substrate, unlike a building which is placed on top of the substrate (soil). This also means that there is an acoustic impedance mismatch between the soil and the building which does not exist in the mesa system. Thus, earthquakes passing through buildings do not seem to be similar enough to the mesa system to allow any accurate comparisons to be made about how the waves propagate through the raised structure.

Chapter 4

Device Fabrication

This work was performed at the University of Waterloo's Quantum NanoFab (QNF) facility. The fabrication flow for the entire polariton device is shown in Fig. 4.1. For the ZnO/GaAs velocity measurement device, parts (b) and (c) apply. For the GaAs velocity measurement device and the $LiNbO_3$ IDT devices, only part (c) is relevant, as the IDT fabrication process is the same as for the polariton devices.

4.1 Electron Beam Lithography

When starting this work, the IDT design was not yet set and was designed to have a wavelength of 4 μm, which meant that the width of the fingers and the spacing between them was 1 μm. The mask alignment system in QNF was not capable of meeting these needs, and would require a new mask for any IDT redesign, so EBL was necessary.

4.1.1 Resist Coating

Before coating a sample with e-beam resist, it was cleaned by placing it in acetone for 5 minutes and then rinsing the acetone off with isopropyl alcohol (IPA). Two different concentrations of poly(methyl methacrylate) (PMMA) 950K in anisole were used as e-beam resist. A concentration of 3% PMMA in anisole is called A3; larger PMMA concentrations give thicker resist and thus require a larger dose to fully develop. For the IDT fingers, PMMA A6 was used in order to have higher side-walls; the purpose of this was to make the lift-off process easier. PMMA A3 was used for the IDT busbars, since there were no

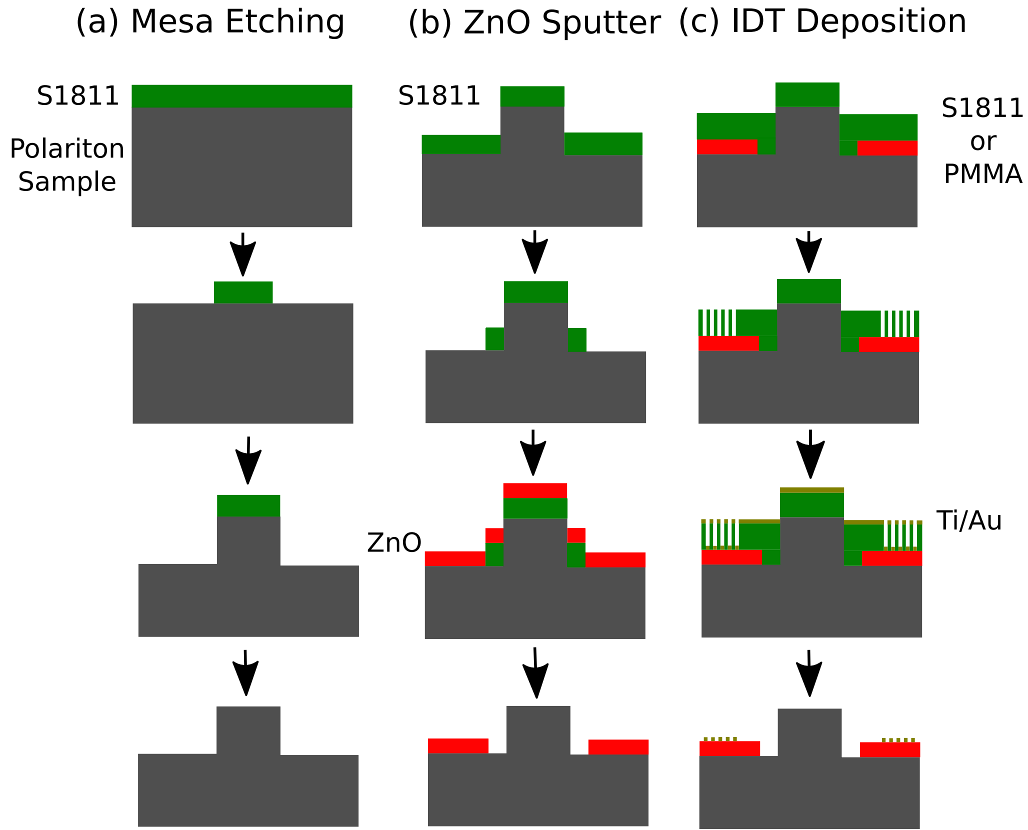

Figure 4.1: Fabrication flow for polariton device, including (a) Mesa etching, (b) ZnO deposition with liftoff and (c) IDT deposition. Step (a) was skipped in non-polariton devices.

issues with lift-off with such large features and the thinner resist reduced the necessary exposure time.

The recipe used for PMMA A3 and A6 was similar, with only the peak spin speed differing between them. Samples were baked on a hot-plate at 180°C for 5 minutes prior to the resist coating. The sample was placed on a spin-coater and resist was applied using a disposable pipette, covering the entire sample. The sample was spun for 1 second at 1000 rpm, ramping up that speed by 200 rpm/s. Then the speed was ramped up by 1500 rpm/s to reach the peak spin speed and allowed to spin for 35 seconds. After the spinning, the sample was baked on a hot-plate at 180°C for 20 minutes.

For PMMA A3, the peak speed was 4000 rpm, while it was 5000 rpm for PMMA A6. The slower peak speed for PMMA A3 produces a slightly thicker resist layer, which is beneficial when it is only 150 nm thick, since it allows for slightly thicker metal deposition. The faster peak speed for PMMA A6 produces a slightly thinner resist layer, since the 450 nm thick layer is already thick enough for the intended purpose and thicker resist requires a larger dose.

4.1.2 Exposure

The PMMA A3 and A6 resist layers were used for different purposes, and therefore, different parameters were used during the exposure; these parameters are detailed in Table 4.1.

Table 4.1: EBL Exposure Parameters

Parameter	PMMA 950K A3	PMMA 950K A6
Aperture	60 μm	30 μm
Acceleration voltage	10 kV	25 kV
Dose	100 $\mu C/cm^2$	350 $\mu C/cm^2$
Step size	100 nm	20 nm
Writefield size	100 μm^2	100 μm^2

The main differences are the dose and the accelerating voltage. In EBL, the higher the accelerating voltage, the further the electrons penetrate into the substrate below the resist. This decreases the amount of forward scattering of electrons in the resist, which accounts for most of the exposure, so the dose must be increased. The advantage of a higher accelerating voltage is that resolution is improved, since the unexposed areas will be less effected by forward scattering of electrons. A larger aperture increases the beam current and thus decreases the time necessary for a dose. The step size must change to ensure that the beam speed is less than 10 mm/s; high beam speeds make the beam placement less accurate.

4.1.3 Development

Development was done with 1:3 methyl isobutyl ketone (MIBK):IPA solution available in the cleanroom. The sample was immersed in the MIBK:IPA solution for 30 seconds while being lightly agitated. Immediately afterwards, the sample was immersed in IPA for 30 seconds, which stops the development of the PMMA. The sample was blow-dried with N_2.

4.1.4 Descum

Before metal deposition, a descum of the sample is absolutely necessary to remove any resist residue remaining on the patterned areas. The necessity of this was proved by several failed devices at the beginning of fabrication, where the deposited metal came off the sample along with the resist during the lift-off process.

For the descum, low power O_2 plasma etching was used. The etching was done at at 25°C under a pressure of 100 mTorr, with 50 W of RF power applied. For PMMA A3, the descum was only done for 10 seconds, to minimize the change in resist thickness. The descum for PMMA A6 was done for 20 seconds; while it may not be necessary to do for 20 seconds, the A6 can handle a longer descum than the A3 without becoming too thin.

4.1.5 Metal Deposition

Metal deposition was done with e-beam evaporation, as opposed to sputtering, to make lift-off feasible. By evaporating at a pressure of 4.0×10^{-6} Torr or lower, deposition is line-of-sight; this minimizes the amount of metal deposited on the undercut area and on the sidewalls of the resist.

For the IDT fingers, 20 nm of titanium (Ti) and 20 nm of gold (Au) were evaporated; the Ti was used as an adhesion layer while the Au provides a non-oxidizing contact. For the busbars, made in a separate step after the fingers, 20 nm of Ti and 60 nm of Au were used.

4.1.6 Lift-off

Lift-off was done in Remover-PG, an N-methyl-2-pyrrolidone (NMP)-based solvent. Generally, samples can be left in Remover-PG overnight to complete the lift-off, but this did not work well for the patterns used in this work. The method used here is to heat the Remover-PG on a hot-plate (at 80-90°C) and leave the sample in the warm solvent for 15-20 minutes. Once the resist has swollen up (producing visible bubbles on the formerly smooth surface), the sample can be agitated to release the resist from the surface.

With a GaAs substrate, heavy ultrasonication is not recommended, as it will eventually cause the sample to break. The agitation used successfully for this work involved short periods of sonication (5-10 seconds) using a portable ultrasonicator. The portable ultrasonicator is less powerful than the sonicator built into one of the wetbenches, which is often used for sonication of robust silicon samples.

Once the sample appeared to be clear of resist, it was rinsed off with IPA and blow-dried with N_2. In the rare case that there was still resist remaining between the IDT fingers, the sample is placed back into the Remover-PG and the above process was repeated. Complete IDTs on both GaAs and ZnO/GaAs are shown in Fig. 4.2.

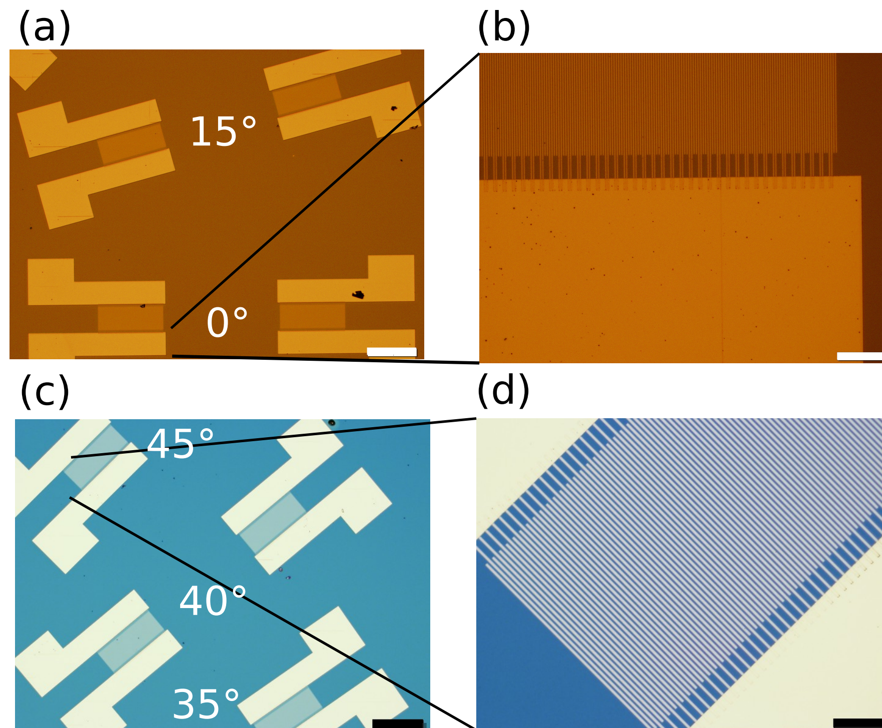

Figure 4.2: (a) IDTs on GaAs at 0° and 15° from the [110] direction. Scale bar is 200 μm. (b) 0° IDT from left side. Scale bar is 20 μm. (c) IDTs on ZnO/GaAs at 35°, 40° and 45° from the [110] direction. Scale bar is 200 μm. (d) 45° IDT from left side. Scale bar is 20 μm.

4.2 Optical Lithography

At the end of 2017, a maskless aligner (MLA) was installed in QNF, which can be used to make patterns with dimensions down to 1 μm. In addition, designs could be changed at any time before patterning, which allows for greater flexibility. In order to decrease fabrication

time and increase the number of devices, this method was used almost exclusively for work for this thesis in 2018.

4.2.1 Resist Coating

As with the e-beam resist in section 4.1.1, the sample was cleaned with acetone and rinsed with IPA before resist coating. Two different types of photoresist were used, depending on the pattern being written. S1805 was used when patterning IDT fingers, while S1811 was used when patterning IDT busbars. As with EBL, the resist used for the IDT fingers is thinner than the resist used for the busbars.

The same recipe was used for both resists. The sample was placed on a spincoater and resist was applied to cover the entire sample. The sample is accelerated by 100 rpm/s to reach 500 rpm, which it spins at for 5 seconds. The speed is then ramped up to 5000 rpm at 500 rpm/s, where it spins for 60 seconds. After the spinning, the sample is baked for 90 seconds on a hotplate at 110°C.

4.2.2 Exposure

The MLA uses a laser to expose the photoresist, with a 405 nm and a 375 nm laser available. For this work, the 405 nm laser was used. As in EBL, a dose is specified instead of an exposure time. The dose used for S1805 was 75 mJ/cm^2 while the dose for S1811 was 100 mJ/cm^2. A measure of the focus distance of the laser, called defocus, is also specified; for both S1805 and S1811, a defocus of 0 was used.

4.2.3 Development

Development was done with the developer MF-319. The sample was immersed in MF-319 and lightly agitated for 45 seconds, after which it was placed in DI water for 60 seconds. The sample was then blow-dried with N_2.

4.2.4 Subsequent Steps

The descum was done in the same manner as described in section 4.1.4. Only the 20 second descum used, as even the S1805 is thicker than the PMMA A6.

The metal deposition and lift-off steps were identical to those described in sections 4.1.5 and 4.1.6, respectively.

The IDTs made with the MLA are shown in Fig. 4.3. (a) and (b) are from a polariton device, (c) is from a doped QW device (M630) and (d) is from a Lieb lattice device on $LiNbO_3$.

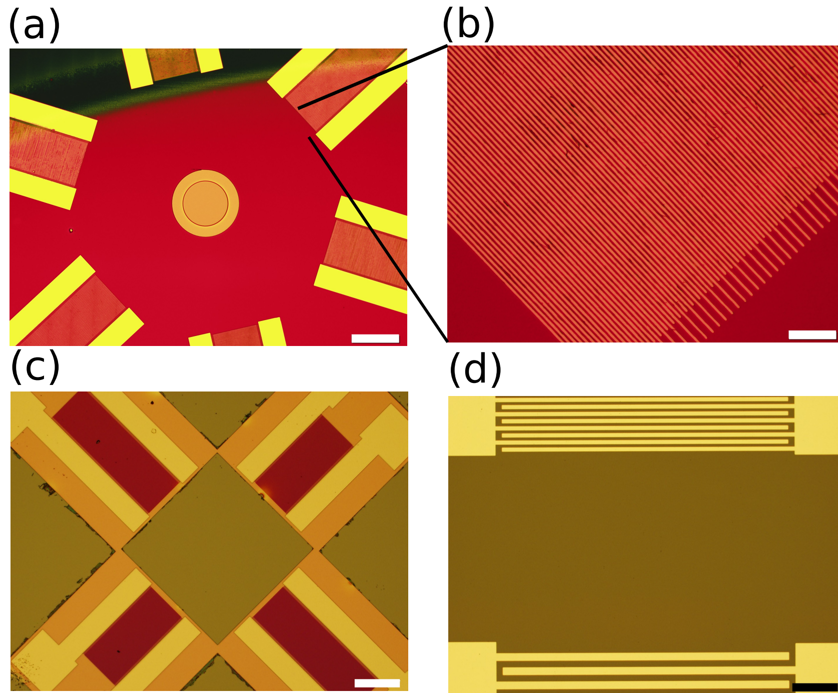

Figure 4.3: (a) IDTs on ZnO around circular mesa with diameter 200 μm. Scale bar is 200 μm. (b) IDT along [100] direction seen in (b), before busbar patterning. Scale bar is 20 μm. (c) IDTs along [100] direction on doped QW sample, on top of islands consisting of, from bottom to top, Ti/Au/ZnO. Scale bar is 200 μm. (d) IDTs along X'direction on $LiNbO_3$. Scale bar is 200 μm.

4.3 Troubleshooting Lithography Steps

Fig. 4.4 shows some of the problems encountered during the fabrication of the IDT devices. Fig. 4.4(a) shows a problem with patterning of the IDT fingers using EBL; this only

occurred for some angled IDTs. In this case, a corner of every writefield was not exposed properly, cutting off several fingers for each writefield. This was solved by changing the direction that the electron beam moves in, so that it moves parallel to the fingers instead of perpendicular to them. This makes the write process slower, but it works as expected every time.

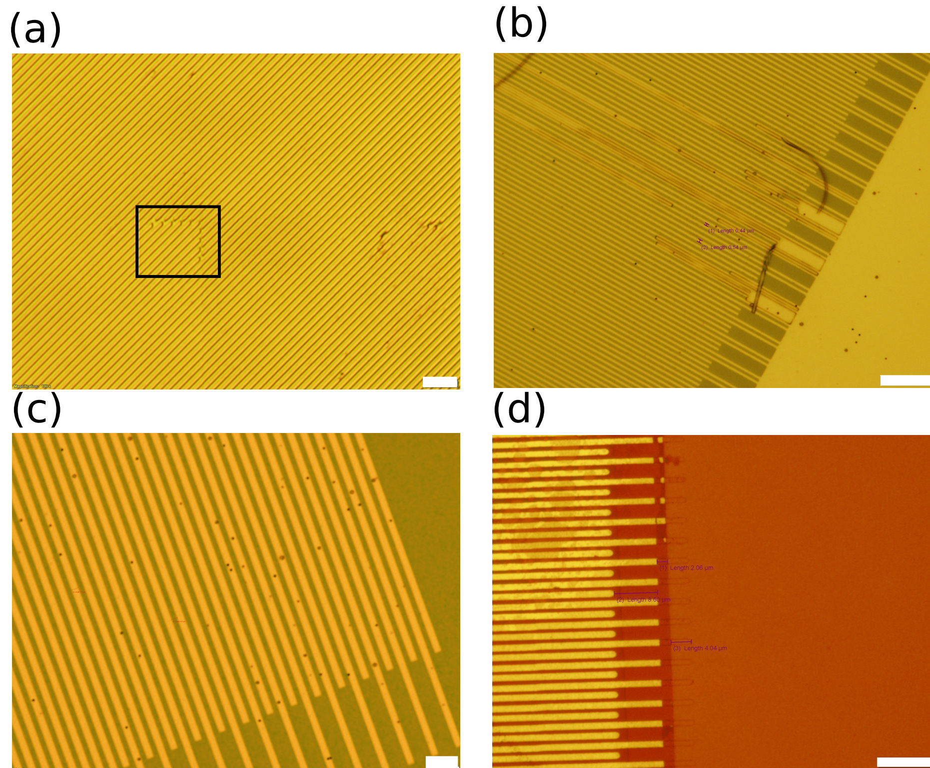

Figure 4.4: Illustration of various problems encountered during fabrication. (a) Corner of EBL writefield was not properly exposed. This occurred for every writefield used for the fingers. Scale bar is 5 μm. (b) Incomplete lift-off of IDT fingers. Scale bar is 10 μm. (c) Black dots on IDT fingers. Scale bar is 5 μm. (d) Etching of Al IDT fingers and ZnO by photoresist developer. The colour changes indicate etched areas. Scale bar is 10 μm.

Fig. 4.4(b) shows an issue with the lift-off of the metal between the IDT fingers. For 4 μm IDTs, it was often the case that lift-off was incomplete, even after harsh lift-off procedures. This was a problem specific to IDTs made in a single step, and was resolved by implementing the two-step process mentioned above.

In Fig. 4.4(c), there are black dots on the metal fingers after lift-off. This turned out to be due to the evaporation speed of Au. When Au is evaporated at rates above 1.0 Å/s, small lumps of Au will form on the surface, which are seen as black spots when viewed with bright-field microscopy. This is not a critical issue, but is solved by evaporating the Au at a slower rate, such as 0.7 Å/s.

The busbar lithography step has not gone as expected in Fig. 4.4(d). The Al fingers have been etched away, in addition to the ZnO layer underneath the IDT fingers. This is due to the use of photoresist developers such as MF-319, which contain KOH^-, an etchant of both of these materials. This makes photolithography-based double-step IDT development incompatible with Al IDTs. In order to protect the ZnO, a layer of PMMA can be applied before the photoresist and then removed with the descum step.

4.4 Mesa Etching

Etching of the mesa was done with inductively-coupled plasma (ICP) reactive ion etching (RIE). Several etching recipes for GaAs were tested to find the best etching rate. Ultimately, the recipe shown in Table 4.2 was selected, which gives an etch rate of 2.596 nm/s. For the desired etch depth of 1951 nm, this gives an etch time of 751.54 s, or 12 minutes 31.54 seconds. Use of a faster etch rate could potentially lead to over or under-etching, as small errors in the measured rate would accumulate. The results of this etching are seen in Fig. 4.3(a).

Table 4.2: DBR Etching Recipe

Parameter	Value
ICP Power	500 W
RF Power	50 W
Temperature	25°C
Etch Pressure	5 mTorr
Ar	33 sccm
Cl_2	2.6 sccm
BCl_3	4.4 sccm

4.5 ZnO Sputtering

ZnO was sputtered in an RF magnetron system. A 2" ZnO target was used. The substrate was heated to 100°C and rotated at 60 rpm. An RF power of 100 W was used during the deposition process.

In the initial attempts, a deposition pressure of 3 mTorr was used with a flow of 27 sccm Ar gas. While the resulting ZnO film was c-axis oriented, as indicated by X-ray diffraction (XRD), it was not piezoelectric, as IDTs on the ZnO surface did not work. The issue was identified as a lack of oxygen in the film. In order to solve this problem, changes to two sputtering parameters and an additional post-sputtering step were tested.

The first step was to add oxygen gas during the sputtering process; this is called reactive sputtering. The gas flow was kept constant at a total of 27 sccm, while a 60:40 ratio of Ar to O_2 was used; this meant 16.2 sccm Ar and 10.8 sccm O_2. This film was not piezoelectric either, so another change had to be made. An increase in deposition pressure from 3 mTorr to 10 mTorr or a post-sputter annealing step in O_2 or both together were tested. The annealing is done in a separate chamber under pure O_2 flow at 300°C for 30 minutes.

All of the combinations look the same when examined with XRD, as shown in Fig. 4.5. However, unlike the previous process, all combinations of the changes were found to yield a piezoelectric ZnO film, with the SAW velocity along the [110] direction of GaAs similar in all cases, as shown in Fig. 4.6. The fact that SAWs propagating on both ZnO films sputtered at 10 mTorr made that measurement more reliable, compared to the film sputtered at 3 mTorr. In addition, the annealing process requires the sample to be completely clear of all organics including photoresist; this is sometimes an issue, as shown by the remaining resist in Fig. 4.3(c). Based on the sharpness of the s11 response and to simplify the fabrication process, the method using 10 mTorr deposition pressure and no annealing was chosen.

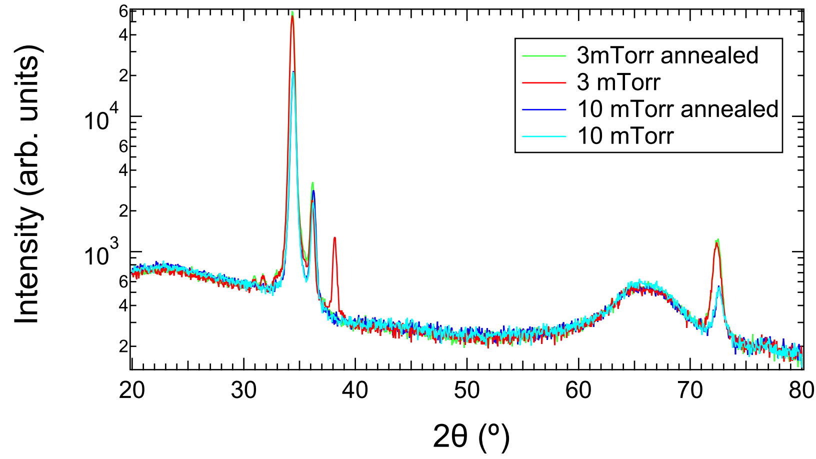

Figure 4.5: XRD spectra from ZnO samples sputtered at 3 mTorr and 10 mTorr, annealed and not annealed. A 2° offset was used to remove the GaAs substrate peaks. The main peaks at 34.35° and 72.35° correspond to the (002) and (004) planes of ZnO, respectively.

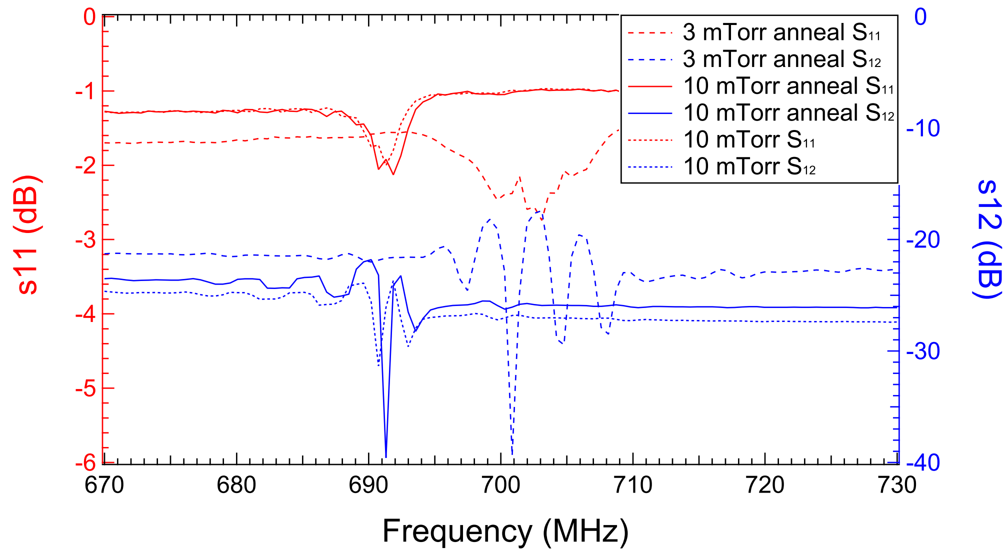

Figure 4.6: Comparison of reflection and transmission for IDTs on ZnO/GaAs in [110] direction, with different treatment of the ZnO.

Chapter 5

Results

This section presents the results of IDT electrical measurements, characterization of the temperature and direction dependence of the SAW velocity and optical measurements of the effect of SAWs.

5.1 IDT Quality Measurement

The IDTs are tested by measuring the S-parameters, also referred to as the reflection and transmission spectra, using a network analyzer. Aside from determining if SAWs are being generated, what the resonance frequency of the IDT is and how much of the applied power is being reflected back, the responses also reveal other facts about the SAW propagation. The double finger IDTs in Fig. 5.1(a) show a response around 706 MHz, with an S_{11} depth of ~0.5 dB. The responses of IDTs with the same number of finger pairs and aperture, but with a single finger design instead of a double finger design, are shown in Fig. 5.1(b). In this case, the response is around 710 MHz, with an S_{11} depth of ~0.4 dB. However, for the single finger design, the reflections due to the IDT acting as a Bragg reflector create ripples superimposed on the response with a frequency of 2 MHz. Using the measured acoustic velocity (from $\lambda = 4$ μm and the resonant frequency) and the distance between the transmitting and receiving IDTs (500 μm), a ripple caused by reflections should be somewhere between 1.34 MHz and 2.78 MHz. The measured ripple frequency of 2 MHz matches well with this range and implies that the majority of the SAW signal is being transmitted and received closer to the centre of the IDTs than the ends. This also shows that, as expected, the double finger IDT does not reflect the SAW.

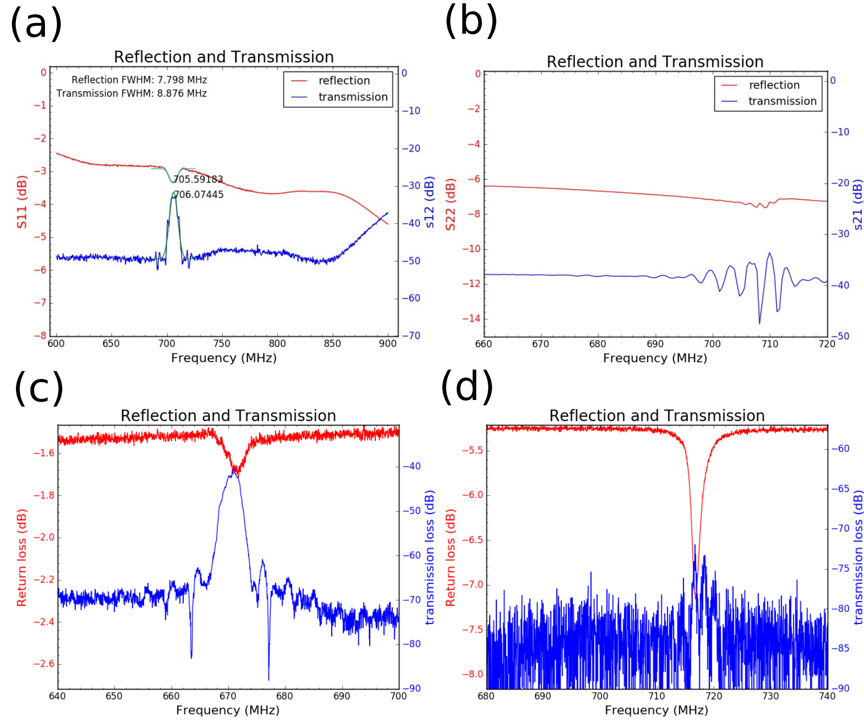

Figure 5.1: IDT reflection and transmission responses. (a) Double finger IDT in [110] direction on GaAs, $\lambda = 4$ μm (b) Single finger IDT om [110] direction on GaAs, $\lambda = 4$ μm (c) Single finger IDT in [110] direction on sample with n+ doped layer 745 nm below surface, $\lambda = 4.196$ μm (d) Single finger IDT in [110] direction on polariton sample with 1950 nm mesa between IDTs, $\lambda = 4$ μm.

Fig. 5.1(c) shows the response of single finger IDTs on a doped substrate. This response is from IDTs on the same substrate at those in Fig. 4.3(c). As can be seen in the measured response in Fig. 5.1(c), SAWs are being generated, but the response is quite weak, with an S_{11} depth of ~0.12 dB. This is similar to the response seen in Ref. [23], which proposed and testing this structure.

Fig. 5.1(d) shows the response of IDTs on a polariton device with a mesa between them. The S_{11} depth is large compared to the other results shown here (~2.0 dB), but the transmission is much smaller. As this is not observed in any of the other devices, it is likely due to the mesa. This does not prove that the SAW can or cannot propagate through a mesa, although it does provide some potential evidence that transmission is possible. The

low transmission is not necessarily an issue for lattice generation, as long as the SAW is strong enough to modulate the bandgap under the mesa.

5.2 GaAs and ZnO/GaAs SAW Velocity Measurement

In order to form different lattices using standing SAWs, the frequency of the SAW should be the same in all directions. In order to design the appropriate IDTs to make this possible, the SAW velocity in all relevant directions on GaAs and ZnO films on GaAs must be known. In addition, since the IDTs will be operating at cryogenic temperatures, the velocity must be known at those temperatures.

The room temperature (RT) data for direction-dependent velocity on GaAs and ZnO/GaAs is available [13, 14, 30], but the temperature dependence of the velocity is not. Due to the symmetry around the [110] direction in GaAs, only the 45° between the [110] and [100] directions need to be measured to fully characterize the system. Pairs of IDTs separated by 500 nm were fabricated in 5° intervals from the piezoelectric [110] direction to the non-piezoelectric [100] direction on both GaAs and a 316 nm ZnO film on GaAs.

The velocity is calculated by multiplying the design wavelength of the IDT by the resonant frequency of the IDT, found from S-parameter measurements. The S_{11} and S_{12} (reflection and transmission) parameters give nearly identical resonant frequencies, although they may differ by 1-2 MHz. For the 4 μm wavelength used, that corresponds to an error of 4-8 m/s, which is at most a 0.29% error from the lowest theoretical velocity of 2720 m/s in GaAs.

The RT results for the velocity measurements are shown in Fig. 5.2, with the filled symbols representing measurements done for this work and the open symbols representing theoretical values from several literature sources. The measured trends coincide with those seen in the literature, but the values do not match exactly. The difference between literature and experimental values is consistent for GaAs, with a difference of at most 22 m/s (0.8%), while the difference is larger and less consistent (up to 116.8 m/s or 4.02%) for ZnO/GaAs. The larger difference for the ZnO/GaAs device is due to the difference in film thickness compared to the available literature data. In Ref. [30], they use a $0.13\lambda_{\text{SAW}}$ thick ZnO film (1.6 μm for $\lambda_{\text{SAW}} = 12$ μm), whereas the film used in these measurements is $0.079\lambda_{\text{SAW}}$ (316 nm).

The downward parabolic curve seen in the GaAs angular dispersion is indicative of an auto-collimating SAW behaviour around the [110] direction, whereas the upward parabolic curve seen in the ZnO/GaAs behaviour is representative of a diffracting SAW [30]. Due to

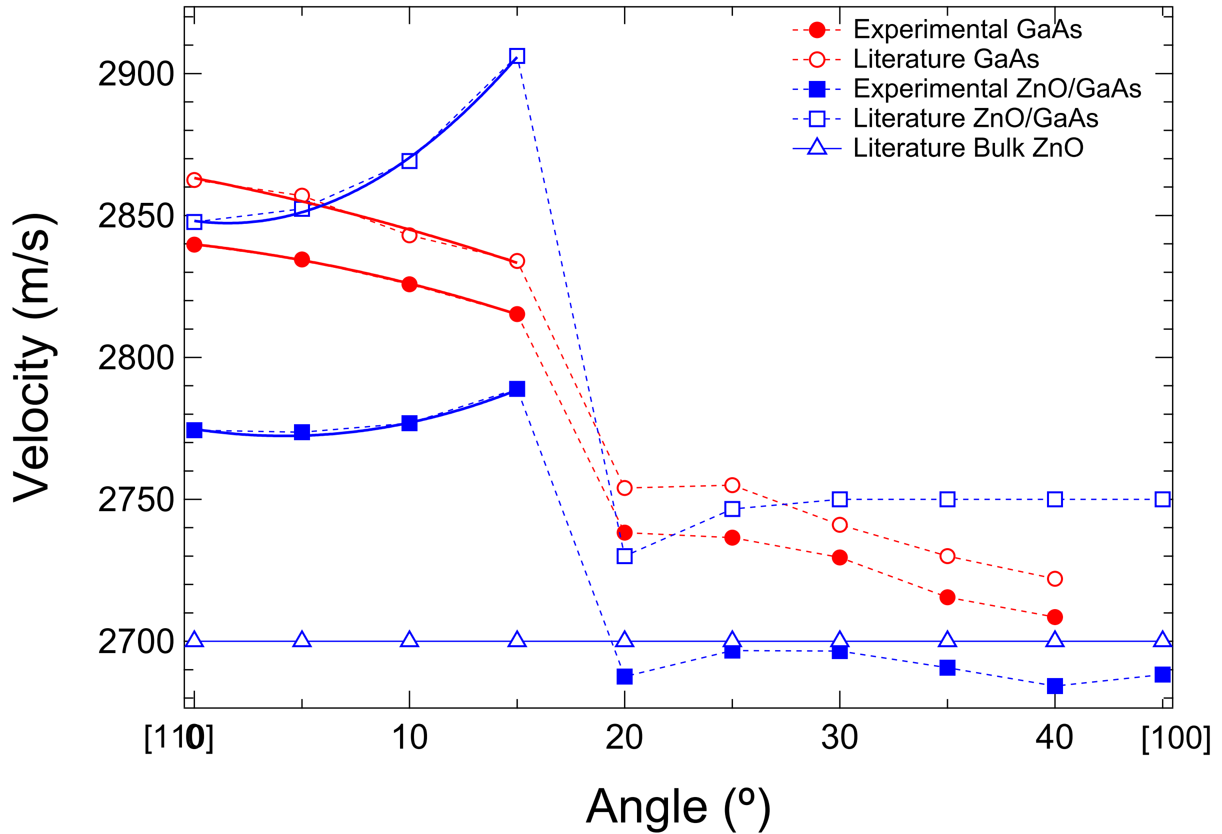

Figure 5.2: Direction dependence of velocity on GaAs and ZnO/GaAs samples, measured at RT. Literature values for GaAs [14] and ZnO/GaAs [30] are shown with new measurements for this work and bulk ZnO values found with COMSOL.

this diffracting behaviour, propagation of SAWs around the [110] direction on a ZnO/GaAs system is not a good choice over long distances (tens of λ_{SAW} or more). Additionally, the division between two sets of velocities, representing the pSAWs and the SAWs, seen in GaAs is reproduced in the ZnO/GaAs device. This indicates that the same division between pSAWs and the SAWs, divided around a point between between $\theta = 15°$ and $20°$, exists on ZnO/GaAs.

The temperature dependence of the SAW velocity was measured by placing the devices in a liquid-helium cryostat with six microwave coax cables, whose base temperature T is 1.4 K, and taking measurements after complete thermalization at each T. In order to maximize

the number of devices per cool-down, we measure the S_{11}-parameters, which requires only one coax cable per device instead of two. Data from the GaAs and ZnO/GaAs devices was collected over a total of five cool-downs. In some cases, signals for several IDTs are too small to be visible, so we are not able to obtain data from all devices. These small signals may be due to impedance mismatch at low temperatures.

Figure 5.3(b) presents representative low temperature angular dispersions of GaAs (red) and ZnO/GaAs (blue) substrates at 1.4 K (closed symbols) and 120 K (open symbols). The angular dispersion behaviors look similar at low temperatures to the RT dispersions; namely, there are regions of faster pSAWs and slower SAWs separated around $\theta = 20°$. In addition, slower SAW modes appear as well as pSAWs in the smaller θ region of the ZnO/GaAs devices.

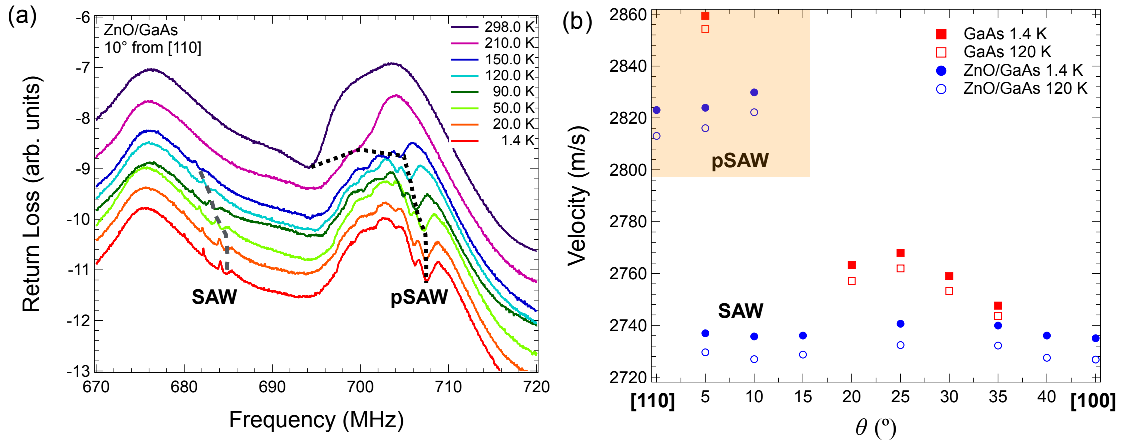

Figure 5.3: (a) Return loss spectra of an IDT on the ZnO/GaAs device at $\theta = 10°$, measured from 1.4 K to 298 K. The change in resonance around 680 MHz and 705 MHz is indicated by dashed lines, corresponding to the SAW and the pSAW modes, respectively. Arbitrary vertical offsets are applied to each spectra for clarity. Cables have not been calibrated out. (b) The velocities seen for bare GaAs and ZnO/GaAs at 1.4 K and 120 K.

The S_{11} spectra of an IDT on ZnO/GaAs at $\theta = 10°$ are shown as an example in Fig. 5.3(a), where two unique resonant signals are seen. Based on the velocity relative to the other IDTs, we associate the lower and higher frequency signals with SAW and pSAW components, respectively. The dashed lines in Fig. 5.3(a) show the points taken as resonance frequencies for the SAW and pSAW components, which are plotted to scale in Fig. 5.4(b). In particular, at $T = 120$ K, the two resonant f values at $\theta = 10°$ are located at 681.962 MHz and 705.548 MHz, corresponding to v of 2727.85 m/s and 2822.19

m/s, respectively. Since the velocity of the SAW modes near the [110] direction is nearly constant, these modes in ZnO/GaAs may not diffract like pSAWs. These SAW modes do not appear above 200 K in bulk ZnO crystals, which is associated with an decreased resistivity in ZnO, which damps SAW modes [31]. As both GaAs and ZnO/GaAs samples cool down, the velocity values of pSAWs and SAWs increase.

The T-dependent velocities of SAWs and pSAWs are plotted for GaAs (Fig. 5.4(a)) and ZnO/GaAs (Fig. 5.4(b)) at specific angles. All data are fitted well with parabolic relations, and the exemplary fitting results are included in Table C.1 in Appendix C. Since the difference in velocity values is consistent at different θ values (Fig. 5.4(b)), we are able to interpolate v values at any temperatures by applying appropriate pSAW or SAW parabolic relations to the RT velocity data. Using this knowledge, appropriate IDTs can be designed for the planned lattice devices, assuming a ZnO thickness ratio close to 0.08λ.

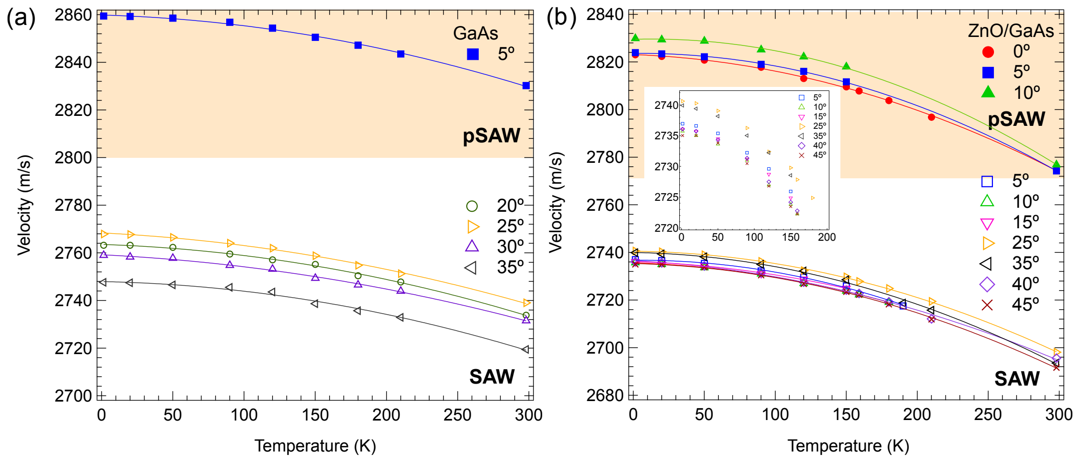

Figure 5.4: Temperature dependence of the SAW and pSAW velocities on (a) GaAs and (b) ZnO/GaAs devices. Lines are parabolic fits to data. Maximum change from RT to 1.4 K is (a) 1.08% and (b) 1.79% of RT velocity for both pSAW and SAW groups. Inset in (b): Magnification of SAW data from 1.4 K to 200 K.

5.3 Optical Measurement of Polariton Devices

The optical path travelled by the photons produced by PL is indicated by the red line in Fig. 5.5. The spectrometer at the end of the path on the right is used to spectrally

resolved the PL data, but one of the mirrors in the path (indicated with blue circles) can also be used to capture images in the near-field or far-field with a charge-coupled device (CCD) camera. The setup uses side-pumping to avoid having to filter out the laser signal from the luminescence.

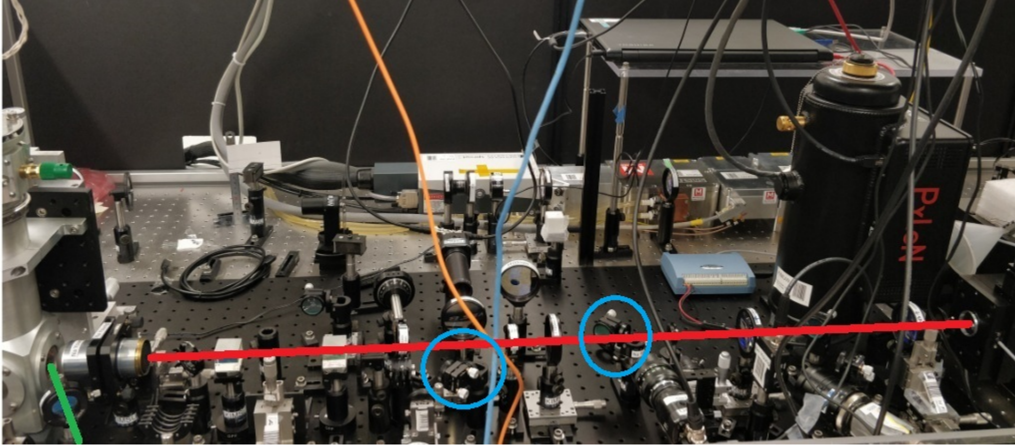

Figure 5.5: Optical table where polariton measurement setup is located. The red line represents the luminescence path after exiting the objective lens. The green line indicates the path that the laser applied to the sample takes; this is used for side pumping. The blue circles indicate mirrors that can be used to image the sample with CCD cameras.

The bandgap modulation produced by the strain associated with the SAW is cyclic when a travelling SAW is used, with minima and maxima. When the bandgap modulation is large enough, it creates an observable splitting of the PL peaks [29]. In order to investigate if the SAWs produced by the fabricated IDTs would effect the excitons as expected, devices were fabricated on QW samples with and without microcavities and the QW peak was observed. The result of this is shown in Fig. 5.6. In Fig. 5.6(a) and (b), the PL peaks before application of a SAW are shown, for a device without and with a microcavity, respectively. The results of applying a SAW with applied power of 16 dBm and frequencies of 690 MHz and 724.5 MHz, respectively, are shown in Fig. 5.6(c) and (d). Based on Ref. [29], this should be a large enough power to see at least some indication of peak splitting.

There is a slight red-shift, peak-broadening and decrease in intensity associated with the application of the SAW, but no peak-splitting. The other symptoms point to a heating effect caused by the SAW, but as the peaks maintain their shape, it suggests that this heating is not enough to dissociate the excitons. The lack of peak splitting means that the

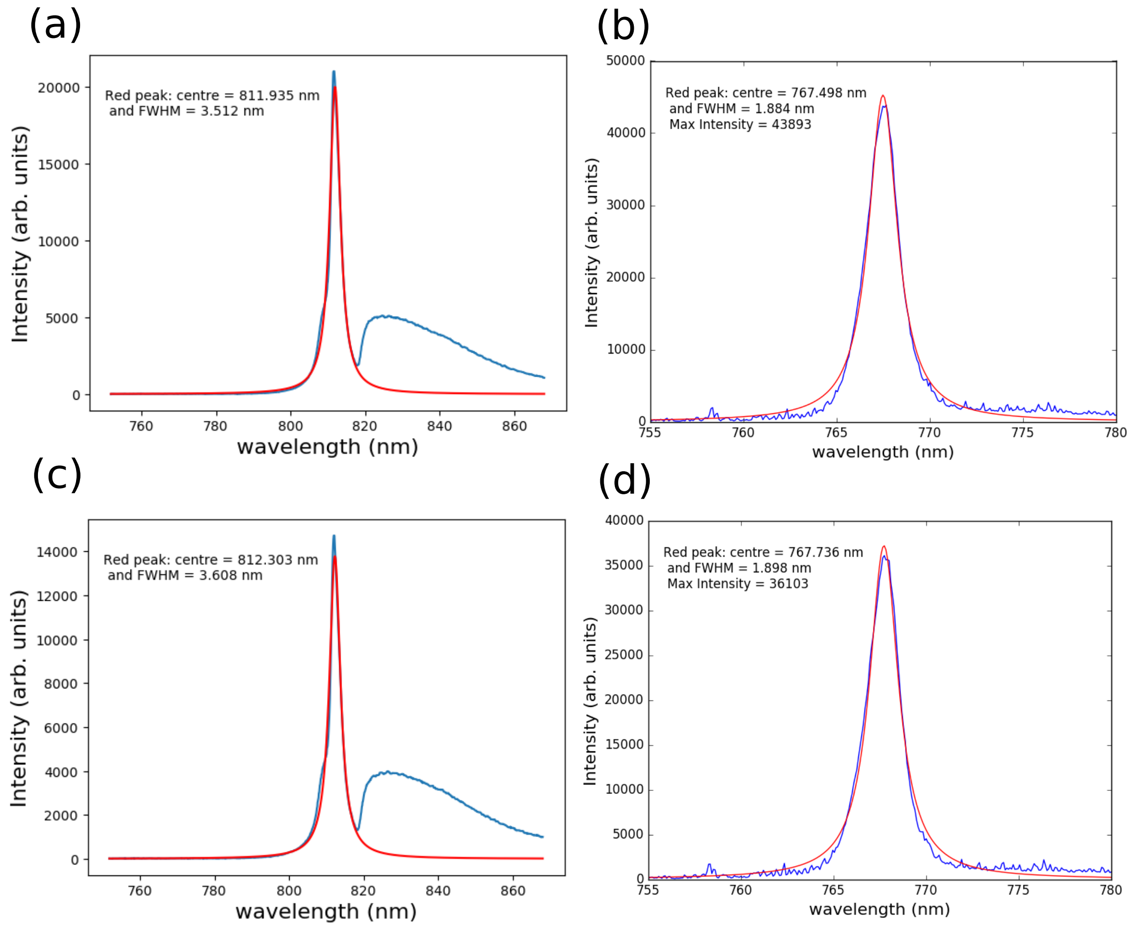

Figure 5.6: Effect of SAWs on excitons in QWs. (a) QW PL peaks of a sample with two 18 nm QWs, 55 nm below the surface. (b) QW PL peaks of the G0299 polariton sample shown in Fig. 2.5. (c) The peak in (a) when a 16 dBm, 690 MHz signal is applied to an IDT. (d) The peak in (b) when a 16 dBm, 724.5 MHz signal is applied to an IDT. The expected splitting due to the application of SAWs is not observed.

SAWs are not strong enough, so detecting lattices formed in the polariton devices is not possible.

5.4 Microfluidic Lattice Formation Measurement

In order to test the lattice formation devices shown in section 3.1.3, an aqueous solution containing latex beads is pipetted in the centre of the IDTs and covered with a piece of a glass microscope slide, as shown in Fig. 5.7(a). In this case, in order to maximize the SAW strength, the strongly piezoelectric $LiNbO_3$ substrate is used.

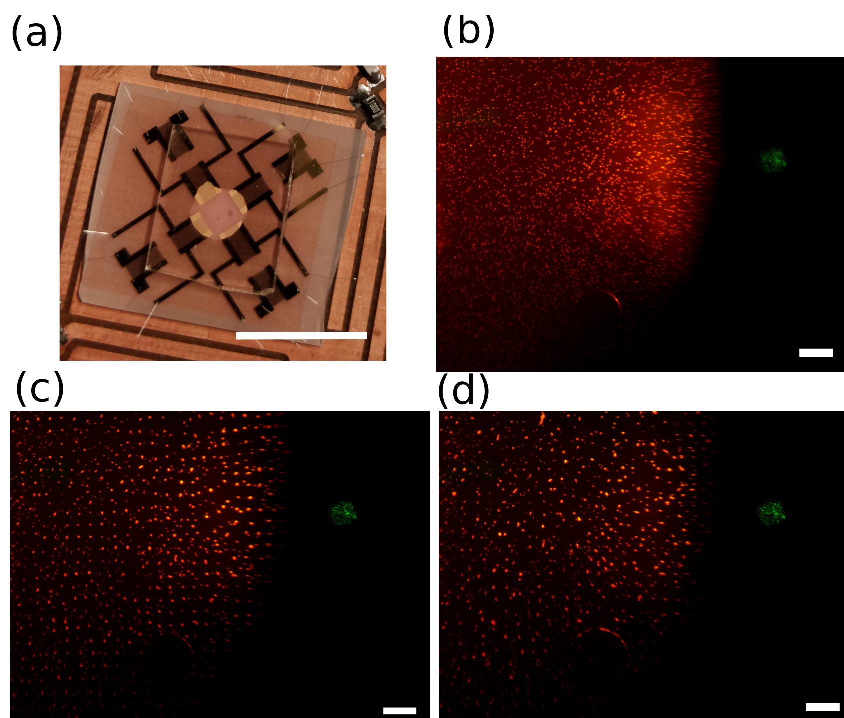

Figure 5.7: Creation of a square lattice of latex beads in aqueous solution with SAWs. (a) Image of latex bead suspension on SAW device; the light area in the centre is the aqueous solution. Scale bar is 2 cm. (b) Fluorescence imaging of uniform distribution of latex beads, before SAWs are applied. (c) Same area as in (b), during application of 58 MHz SAWs with applied power of 13.5 dBm. A partially filled square lattice is formed. (d) Image in (c) during application of 21.65 dBm, 29 MHz SAWs in addition to the 58 MHz SAWs. Scale bar is 120 μm in (b)-(c).

In order to observe the latex beads, a fluorescence imaging system is required. The most common way of capturing such images is via a microscope, but as there was no such microscope available, we built a rudimentary system, as shown in Fig. 5.8. A 532 nm laser

enters the system from the bottom of the image and follows the green line, being reflected by a dichroic mirror. The reflected light is focused onto the sample by a 10x objective lens, shown at the end of the green line. The fluorescence response, which is in the red region of the spectrum (~610 nm), passes through the dichroic mirror instead of being reflected by it. It is then passed through a long pass filter (LPF) to remove the 532 nm excitation signal and imaged with a CCD camera, as shown by the red line.

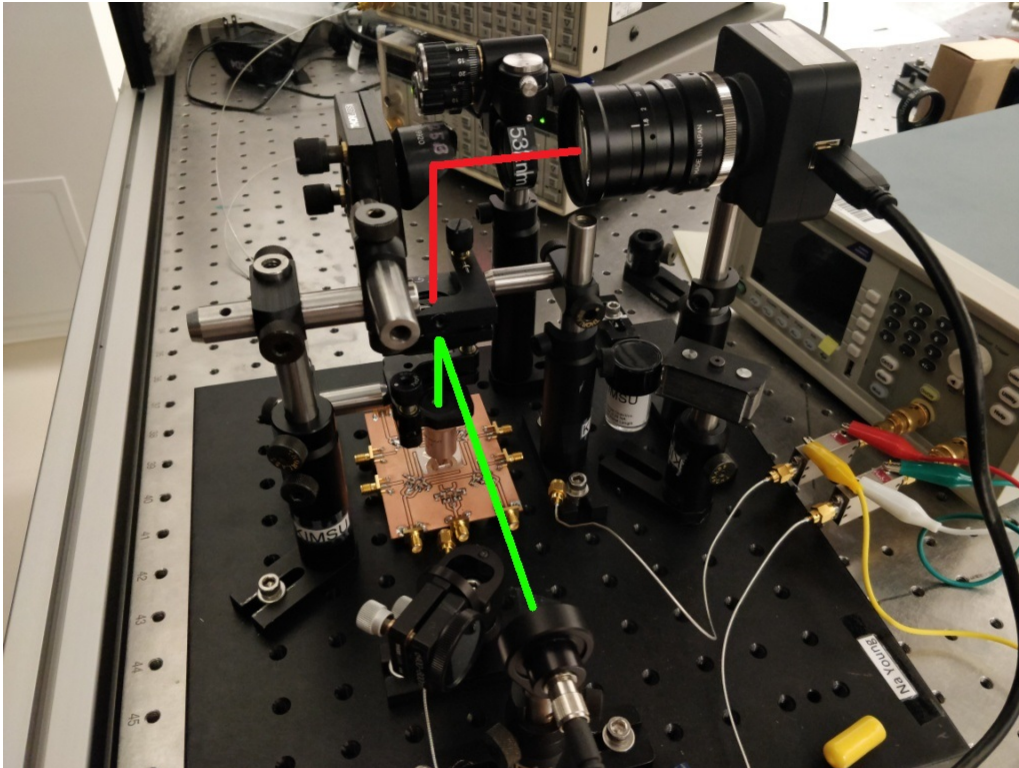

Figure 5.8: Fluorescence microscopy setup to measure lattices formed with latex beads. The green lines show the excitation path, while the red lines follow the fluorescence.

The result of applying a SAW to this latex bead suspension is shown in Fig. 5.7(b)-(d). While the beads are spread out approximately uniformly in Fig. 5.7(b), Fig. 5.7(c) shows the formation of a square lattice when an 13.5 dBm, 58 MHz signal is applied to each of the 58 MHz, 45° IDTs on the $LiNbO_3$ device. The spacing between adjacent points in the lattice is approximately half of the SAW wavelength of 61.6 μm, as expected with a standing wave pattern. In Fig. 5.7(d), the 29 MHz SAW with a power of 21.65 dBm per

IDT is applied in addition to the 58 MHz signal. Contrary to expectations based on the numerical calculations in section 3.3.1, a Lieb lattice does not form. Instead, the previous square lattice becomes slightly disordered and the beads at individual lattice nodes undergo rotation. This may be due, at least in part, to the latex beads being bound to the $LiNbO_3$ surface due to strong surface static charge [22], or possibly to the glass as well.

With these results, it is not yet clear whether the lattice formation idea presented in section 3.1.3 works or not.

5.5 Future Work with Fabricated Devices

While the effect of the SAWs on polaritons was not observed, it has been shown to be possible by at least one other group [21]; therefore, this problem should be solvable. The next task that should be undertaken is to experimentally test the validity of using a mesa to increase SAW strength. Depending on why the effect on the polaritons is not observed, this may require fabrication of IDTs on new samples. In addition, the Lieb lattice and kagome lattice layouts should be tested with polaritons.

The microfluidic approach to testing the lattice formation ideas is promising, but requires some refinement of the measurement setup. In order to make measurements simpler and more consistent, the glass cover should be replaced with a polydimethylsiloxane (PDMS) chamber, as demonstrated in Ref. [32]. A PDMS chamber should also reduce the number of latex beads bound to the $LiNbO_3$ surface, since the chamber will have a height dimension.

Chapter 6

Conclusion

6.1 Summary

The overall goal of this work was to make an exciton-polariton based quantum simulator using SAWs to create a dynamic lattice potential. This thesis lays the foundation for this goal with by studying the IDT design and layout required as well as simulations of the new ideas proposed. Fabrication of a first generation of devices is done, with some promising results.

IDTs of the desired frequencies were designed, fabricated and tested. This included IDTs for 4 μm SAWs on GaAs and ZnO/GaAs, as well as 120 μm and 60 μm IDTs on $LiNbO_3$. Layouts of these IDTs to form a 2D Lieb lattice as well as a kagome lattice were proposed. Numerical calculations were used to show the validity of this approach in the context of particles suspended in a fluid. Numerical calculations and a COMSOL simulation were used to show how a mesa could be used to increase the SAW power available at the QW level of polariton samples.

The equipment necessary to use these IDTs to create lattices, which includes coax cables in a cryostat and a set of power dividers to facilitate the formation of standing waves, was designed and/or built. The process used to fabricate the IDT devices was described in detail, including both a process using EBL and a process using several a maskless aligner, as well as problems that had to be solved in order to make fabrication possible.

The measurement of IDT electrical characteristics was discussed, along with the information about reflection of SAWs that can be gained from such measurements. The characterization of both angular dispersion and temperature dependence of SAW velocity

for GaAs and ZnO/GaAs devices was presented. The room temperature angular dispersion trends coincide with those seen in previous work, and those trends are preserved as the device is cooled down. Slower SAW modes appeared below 200 K for several IDT directions on ZnO/GaAs that only produce pSAWs at room temperature.

Measurements of the effect of the SAWs on excitons in QWs were presented; in this case, the effect was not observable, so another system using latex beads in an aqueous solution was used to test the proposed lattice formation layouts. The test of a Lieb lattice formation device using fluorescence microscopy was presented. While successful in forming a square lattice, the Lieb lattice did not appear, most likely due to the method used to contain the latex bead suspension.

6.2 Future Experiments

Once the problems with the exciton-polariton device are resolved, the next step is to use the device as a quantum simulator. Both the Lieb lattice and the kagome lattice can be used to study flat band formation. The kagome lattice can be used to study geometric frustration. The results could be compared to other work using Lieb or kagome lattices, but the added ability to vary the potential strength during the experiments would be a novel feature that is not possible in other systems, to the best of our knowledge.

The microfluidic work could potentially be useful beyond being a test platform for lattice formation. When the acoustic wavelength is nearly equal to the diameter of the suspended particle, single particles can be trapped at each potential well [32]. In this case, interparticle interactions (Bjerknes forces) and the potential landscape both contribute to the lattice formation. These interparticle trapping scheme may allow the microfluidic system to be used as a quantum simulator as well. A significant benefit of the microfluidic approach is that it allows for various different kinds of particles; in addition to the latex beads used in this work, various cells can be trapped [26], which could potentially lead to some interesting results in lattices like the Lieb lattice. Smaller particles, such as colloidal quantum dots, could potentially be an interesting platform to explore as well, although single particle trapping may not be possible due to the extremely small SAW wavelength required.

References

[1] I. M. Georgescu, S. Ashhab, and F. Nori, “Quantum simulation,” *Rev. Mod. Phys.*, vol. 86, no. 1, pp. 153–185, 2014.

[2] M. Suzuki, *Quantum Monte Carlo Methods in Condensed Matter Physics.* World Scientific, 1993.

[3] R. Feynman, “Simulating physics with computer,” *Int. J. Theor. Phys.*, vol. 21, no. 6/7, pp. 467 – 488, 1982.

[4] S. Lloyd, “Universal quantum simulators,” *Science*, vol. 273, no. 5278, pp. 1073–1078, 1996.

[5] P. Hauke, F. M. Cucchietti, L. Tagliacozzo, I. Deutsch, and M. Lewenstein, “Can one trust quantum simulators?,” *Rep. Prog. Phys.*, vol. 75, p. 082401, aug 2012.

[6] N. Y. e. a. Kim, “Exciton-polariton quantum simulators,” in *Quantum Simulations with Photons and Polaritons:Merging Quantum Optics with Condensed Matter Physics* (D. G. Angelakis, ed.), ch. 5, pp. 91–121, Springer, 2017.

[7] E. A. Cerda-Méndez, D. Sarkar, D. N. Krizhanovskii, S. S. Gavrilov, K. Biermann, M. S. Skolnick, and P. V. Santos, “Exciton-polariton gap solitons in two-dimensional lattices,” *Phys. Rev. Lett.*, vol. 111, no. 14, 2013.

[8] C. E. Whittaker, E. Cancellieri, P. M. Walker, D. R. Gulevich, H. Schomerus, D. Vaitiekus, B. Royall, D. M. Whittaker, E. Clarke, I. V. Iorsh, I. A. Shelykh, M. S. Skolnick, and D. N. Krizhanovskii, “Exciton Polaritons in a Two-Dimensional Lieb Lattice with Spin-Orbit Coupling,” *Phys. Rev. Lett.*, vol. 120, no. 9, p. 97401, 2018.

[9] G.-B. Jo, J. Guzman, C. K. Thomas, P. Hosur, A. Vishwanath, and D. M. Stamper-Kurn, “Ultracold Atoms in a Tunable Optical Kagome Lattice,” *Phys. Rev. Lett.*, vol. 108, p. 045305, jan 2012.

[10] Wikipedia contributors, "Rayleigh wave — Wikipedia, the free encyclopedia," 2018. [Online; accessed 12-July-2018].

[11] C. Deger, E. Born, H. Angerer, O. Ambacher, M. Stutzmann, J. Hornsteiner, E. Riha, and G. Fischerauer, "Sound velocity of alxga1xn thin films obtained by surface acoustic-wave measurements," *Appl. Phys. Lett.*, vol. 72, pp. 2400–2402, may 1998.

[12] G. L. Dybwad, "C-axis orientation of sputtered zno films," *J. Appl. Phys.*, vol. 42, no. 12, pp. 5192–5194, 1971.

[13] J. M. Deacon and J. Heighway, "Acoustic-surface-wave propagation on gallium arsenide," *Electron. Lett.*, vol. 8, no. 1, pp. 6–7, 1972.

[14] C. M. Flannery, E. Chilla, S. Semenov, and H. J. Frohlich, "Elastic properties of gaas obtained by inversion of laser-generated surface acoustic wave measurements," in *1999 IEEE Ultrasonics Symposium. Proceedings. International Symposium (Cat. No.99CH37027)*, vol. 1, pp. 501–504, IEEE, 1999.

[15] W. D. Hunt, R. L. Miller, and B. J. Hunsinger, "Slowness surface measurements for zero- and five-degree [100]-cut gaas," *J. Appl. Phys.*, vol. 60, no. 10, pp. 3532–3538, 1986.

[16] A. Ballato, T. Lukaszek, D. F. Williams, and F. Y. Cho, "Power Flow Angle and Pressure Dependence of SAW Propagation Characteristics in Ouartz," in *1981 Ultrasonics Symposium*, pp. 346–349, IEEE, 1981.

[17] D. Penunuri and K. M. Lakin, "Leaky Surface Wave Propagation on Si, GaAs, GaP , Al2O3 and Quartz," in *1975 Ultrasonics Symposium*, pp. 478–483, IEEE, 1975.

[18] H. Deng, *Dynamic Condensation Of Semiconductor Microcavity Polaritons.* PhD thesis, Stanford University, 2006.

[19] Y. Takagaki, E. Wiebicke, P. V. Santos, R. Hey, and K. H. Ploog, "Propagation of surface acoustic waves in a GaAs/AlAs/GaAs heterostructure and micro-beams," *Semicond. Sci. Technol.*, vol. 17, pp. 1008–1012, sep 2002.

[20] W. C. Wilson and G. M. Atkinson, "Rapid SAW Sensor Development Tools," tech. rep., NASA Langley Research Center, 2007.

[21] E. Cerda-Méndez, D. Krizhanovskii, K. Biermann, R. Hey, P. Santos, and M. Skolnick, "Effects of the piezoelectric field on the modulation of exciton-polaritons by surface acoustic waves," *Superlattices Microstruct.*, vol. 49, no. 3, pp. 233–240, 2011.

[22] C. D. Wood, J. E. Cunningham, R. O'Rorke, C. Wälti, E. H. Linfield, A. G. Davies, and S. D. Evans, "Formation and manipulation of two-dimensional arrays of micron-scale particles in microfluidic systems by surface acoustic waves," *Appl. Phys. Lett.*, vol. 94, p. 054101, feb 2009.

[23] M. Yuan, C. Hubert, S. Rauwerdink, A. Tahraoui, B. van Someren, K. Biermann, and P. V. Santos, "Generation of surface acoustic waves on doped semiconductor substrates," *J. Phys. D*, vol. 50, p. 484004, dec 2017.

[24] B. Villa, A. J. Bennett, D. J. P. Ellis, J. P. Lee, J. Skiba-Szymanska, T. A. Mitchell, J. P. Griffiths, I. Farrer, D. A. Ritchie, C. J. B. Ford, and A. J. Shields, "Surface acoustic wave modulation of a coherently driven quantum dot in a pillar microcavity," *Appl. Phys. Lett.*, vol. 111, p. 011103, jul 2017.

[25] P. Naraine, C. K. Campbell, and Y. Ye, "A SAW Step-Type Delay Line for Efficient High Order Harmonic Mode Excitation," in *1980 Ultrasonics Symposium*, pp. 322–325, IEEE, 1980.

[26] X. Ding, S.-C. S. Lin, B. Kiraly, H. Yue, S. Li, I.-K. Chiang, J. Shi, S. J. Benkovic, and T. J. Huang, "On-chip manipulation of single microparticles, cells, and organisms using surface acoustic waves," *Proc. Natl. Acad. Sci. U.S.A.*, vol. 109, pp. 11105–11109, jul 2012.

[27] I. Bernard, A. A. Doinikov, P. Marmottant, D. Rabaud, C. Poulain, and P. Thibault, "Controlled rotation and translation of spherical particles or living cells by surface acoustic waves," *Lab Chip*, vol. 17, no. 14, pp. 2470–2480, 2017.

[28] F. Guo, Z. Mao, Y. Chen, Z. Xie, J. P. Lata, P. Li, L. Ren, J. Liu, J. Yang, M. Dao, S. Suresh, and T. J. Huang, "Three-dimensional manipulation of single cells using surface acoustic waves," *Proceedings of the National Academy of Sciences*, vol. 113, no. 6, pp. 1522–1527, 2016.

[29] M. M. de Lima and P. V. Santos, "Modulation of photonic structures by surface acoustic waves," *Rep. Prog. Phys.*, vol. 68, no. 7, pp. 1639–1701, 2005.

[30] Y. Kim, W. D. Hunt, Y. Liu, and C. K. Jen, "Velocity surface measurements for zno films over 001-cut gaas," *J. Appl. Phys.*, vol. 76, no. 3, pp. 1455–1461, 1994.

[31] E. B. Magnusson, B. H. Williams, R. Manenti, M.-S. Nam, A. Nersisyan, M. J. Peterer, A. Ardavan, and P. J. Leek, "Surface acoustic wave devices on bulk zno crystals at low temperature," *Appl. Phys. Lett.*, vol. 106, no. 6, p. 063509, 2015.

[32] D. J. Collins, B. Morahan, J. Garcia-Bustos, C. Doerig, M. Plebanski, and A. Neild, "Two-dimensional single-cell patterning with one cell per well driven by surface acoustic waves," *Nat. Comm.*, vol. 6, p. 8686, dec 2015.

APPENDICES

Appendix A

Triangular Lattice Calculations

$$\phi_a = (\cos(\pi/3)kx + \sin(\pi/3)ky) \tag{A.1}$$

$$\phi_b = (\cos(-\pi/3)kx + \sin(-\pi/3)ky) \tag{A.2}$$

$$\phi_c = kx + \gamma \tag{A.3}$$

$$\begin{aligned} PE =& \frac{B_f}{4}((A_a \sin(\phi_a))^2 + (A_b \sin(\phi_b))^2 + (A_c \sin(\phi_c))^2 + \\ & 2A_aA_b \sin(\phi_a)\sin(\phi_b)\cos(\phi_1) + \\ & 2A_aA_c \sin(\phi_a)\sin(\phi_c)\cos(\phi_2) + \\ & 2A_bA_c \sin(\phi_b)\sin(\phi_c)\cos(\phi_1 - \phi_2)) \end{aligned} \tag{A.4}$$

$$\begin{aligned} KE =& 2\frac{B_f}{4}(((A_a \cos(\phi_a))^2 + (A_b \cos(\phi_b))^2) + (A_c \cos(\phi_c))^2 + \\ & 2(2A_aA_b \cos(\phi_a)\cos(\phi_b)\cos(\phi_1)) + \\ & 2A_aA_c \cos(\phi_a)\cos(\phi_c)\cos(\phi_2) + \\ & 2A_bA_c \cos(\phi_b)\cos(\phi_c)\cos(\phi_1 - \phi_2)) \end{aligned} \tag{A.5}$$

$$\psi = \frac{(B_f - B_p)}{B_f} PE - 3\frac{(\rho_p - \rho_f)}{(\rho_f + 2\rho_p)} KE \tag{A.6}$$

where a, b and c represent waves travelling in the 60°, -60° and 0° directions, respectively, γ is the offset of the c wave and ϕ_a, ϕ_b and ϕ_c are factors to shorten the equation length. KE, PE, B_f (B_p) and ρ_f (ρ_p) are the same as described in section 3.3.1.

Appendix B

Additional Strain Depth Equations and Constants

$$\varphi_{SAW} = k_{SAW}x - \omega t \tag{B.1}$$

$$F_x = \frac{\partial \Phi_{SAW}(\vec{r}, t)}{\partial x} \tag{B.2}$$

$$F_z = \frac{\partial \Phi_{SAW}(\vec{r}, t)}{\partial z} \tag{B.3}$$

Table B.1: Constants for Elastic Strain Calculations

Material	v_{SAW} (m/s)	ρ (kg/m^3)	Ω_R	γ_R	ϕ_R	C
GaAs	2863	5316.5	0.501+i0.480	-0.676+i1.154	1.050	0.457
AlAs	3443	3598	0.510+i0.448	-0.756+i1.121	1.082	0.473

These equations and constants are used in section 3.3.2 for strain and electric field calculations. F_x and F_z are the electric field in the direction of propagation and into the substrate, respectively. v_{SAW} is the SAW velocity in the strongest piezoelectric direction and ρ is the density. Ω_R, γ_R, ϕ_R and C are material specific parameters calculated from elastic constants, v_{SAW} and ρ.

Appendix C

Parabolic Fitting Data for GaAs and ZnO/GaAs

Table C.1: Fitting parameters for parabolic relations $v = a\theta^2 + b\theta + c$ or $v = aT^2 + bT + c$ to θ and T dependent data. Data are shown in section 5.2. The θ-data are taken between 0° and 20° in Fig. 5.2. For the $T - v$ data, pSAW and SAW data are selected at $\theta = 5°$ and 25° respectively from Fig. 5.4.

Data	a	b	c
GaAs (θ) [14]	-0.035	-1.46	2863.2
Exp. GaAs (θ)	-0.0525	-0.858	2839.8
ZnO/GaAs (θ) [30]	0.324	-1.01	2848.1
Exp. ZnO/GaAs (θ)	0.138	-1.15	2774.8
pSAW GaAs (T)	-0.00028	-0.017	2859.9
SAW GaAs (T)	-0.00023	-0.030	2759.2
pSAW ZnO/GaAs (T)	-0.00057	0.0035	2823.6
SAW ZnO/GaAs (T)	-0.00045	-0.0066	2740.5